Anomaly-Based Weather Analysis versus Traditional Total-Field-Based Weather Analysis for Depicting Regional Heavy Rain Events

WEIHONG QIAN AND NING JIANG

Department of Atmospheric and Oceanic Sciences, Peking University, Beijing, China

JUN DU

NOAA/NCEP/Environmental Modeling Center, College Park, Maryland

(Manuscript received 4 June 2015, in final form 30 November 2015)

ABSTRACT

Although the use of anomaly fields in the forecast process has been shown to be useful and has caught forecasters' attention, current short-range (1–3 days) weather analyses and forecasts are still predominantly total-field based. This paper systematically examines the pros and cons of anomaly- versus total-field-based approaches in weather analysis using a case from 1 July 1991 (showcase) and 41 cases from 1998 (statistics) of heavy rain events that occurred in China. The comparison is done for both basic atmospheric variables (height, temperature, wind, and humidity) and diagnostic parameters (divergence, vorticity, and potential vorticity). Generally, anomaly fields show a more enhanced and concentrated signal (pattern) directly related to surface anomalous weather events, while total fields can obscure the visualization of anomalous features due to the climatic background. The advantage is noticeable in basic atmospheric variables, but is marginal in nonconservative diagnostic parameters and is lost in conservative diagnostic parameters. Sometimes a mix of total and anomaly fields works the best; for example, in the moist vorticity when anomalous vorticity combines with total moisture, it can depict the heavy rain area the best when comparing to either the purely total or purely anomalous moist vorticity. Based on this study, it is recommended that anomaly-based weather analysis could be a valuable supplement to the commonly used total-field-based approach. Anomalies can help a forecaster to more quickly identify where an abnormal weather event might occur as well as more easily pinpoint possible meteorological causes than a total field. However, one should not use the anomaly structure approach alone to explain the underlying dynamics without a total field.

1. Introduction

A total or full atmospheric variable can be decomposed into its climatic and anomalous components. The former is quasi-stationary and reflects an equilibrium state between solar radiation distribution and geographical features (such as land–sea contrast and large-scale topography), while the latter is a departure from the equilibrium state varying at any moment. For weather analysis, removing the climatic component should result in easier identification of anomalous weather events. Figure 1 is a schematic example in which one can hardly see any anomalous events in the time series of the total variable (the green curve), but it clearly shows two "positive" events and one "negative" event (the red curve) after the climatic component (the dashed curve) is removed. For weather forecasting, those transient weather systems revealed in anomaly fields are the ones causing daily weather changes and, therefore, should be the focus of routine weather forecasts. It is the anomaly part that needs to be predicted, while the climatic part needs only to be understood and known. Although anomaly fields are commonly used in seasonal forecasts (Van den Dool 2007), they are not routinely used in current short-range (1–3 days) weather analyses and forecasts.

However, the usefulness of anomalies in short-range weather analyses and forecasts has been gradually

Corresponding author address: Weihong Qian, Dept. of Atmospheric and Oceanic Sciences, Peking University, Beijing 100871, China.
E-mail: qianwh@pku.edu.cn

DOI: 10.1175/WAF-D-15-0074.1

Publisher's Note: This article was revised on 8 June 2016 to display the correct Eq. (2), which was inadvertently replaced when originally published.

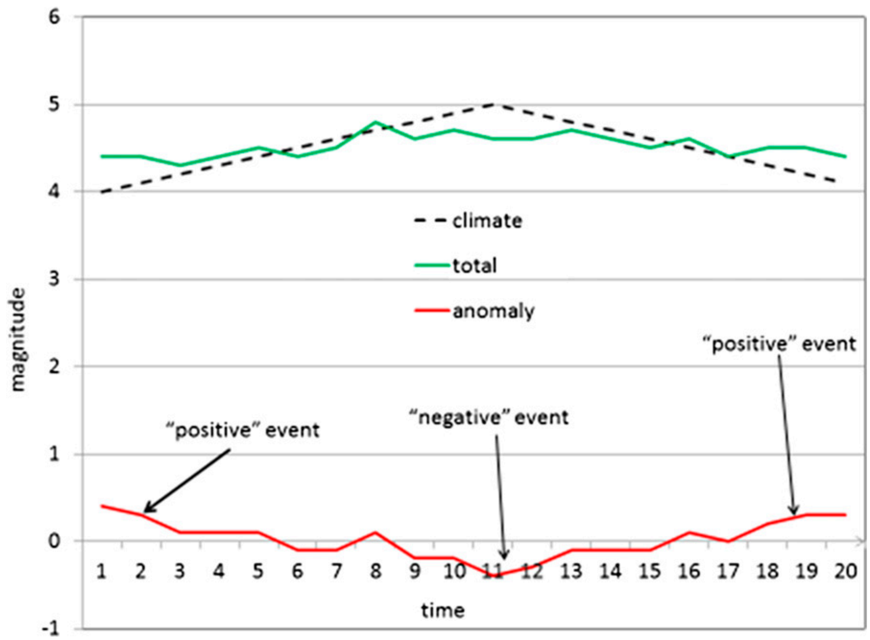

FIG. 1. A schematic diagram of the conversion of a total variable into an anomaly by removing the climatic component to better reveal hidden anomalous weather episodes, where two "positive" and one "negative" anomalous events are shown.

recognized by both research and operational meteorologists. For example, normalized anomaly (NA) or standardized anomaly-based "anomaly forecasts" have been proposed and used in case studies and operations in the last decade for high impact weather events (Grumm and Hart 2001; Hart and Grumm 2001; Junker et al. 2008; Junker et al. 2009; Graham and Grumm 2010; Grumm 2011a,b; Graham et al. 2013). Du et al. (2014) further proposed "ensemble anomaly forecasts" by combining anomaly forecasts with ensemble prediction to quantitatively measure the confidence of an anomaly forecast, which is similar to the idea of an extreme forecast index (EFI) used at the European Centre for Medium-Range Weather Forecasts (ECMWF; Lalaurette 2003; Zsoter 2006). The Storm Prediction Center of the National Centers for Environmental Prediction (NCEP) has been using anomaly-based forecasting for several years, and the staff there have developed a web-based tool (http://www.spc.noaa.gov/exper/envbrowser/) that allows users to evaluate how the current and near-term forecast of environmental conditions compare to climatology for severe weather forecasting (Smith et al. 2012). In recent years, a raw anomaly (RA) based analysis has also been found to be useful in short-, medium-, and extended-range diagnoses and forecasts of extreme weather events such as freezing rain (Qian and Zhang 2012), heat waves (Ding and Qian 2012; Qian et al. 2016), heavy rain (Qian et al. 2013), and typhoon tracking (Qian et al. 2014; Huang et al. 2015). The relationship between the NA and RA is NA = RA/σ, where σ is the climatological standard deviation of a variable. A systematic comparison between RA and NA will be discussed in a separate study. Generally speaking, RA is better in describing the spatial structure related to a surface anomalous weather event, while NA is better in indicating the abnormality of an event relative to climatology. Since the spatial structure of weather systems is a primary interest in this study, RA is used here.

We would like readers to keep the following two things in their mind when they read the paper. One is that this decomposition approach should be considered as an alternative way to present information already contained in the original total field rather than providing any new information as illustrated in Fig. 1. This new way of expression will, however, help forecasters in a meaningful way such as easier identification of anomalous episodes and better visualization of anomalous structures. This could save forecasters time and effort in quickly grasping details related to a high-impact weather event in a time-restriction operational environment. Another is that an anomaly field should not be used alone (without a total field) to interpret the underlying dynamics since atmospheric flow cannot be physically separated into two independent parts (anomaly and climatic background) and any weather phenomenon (such as precipitation) occurs as a result of total flow rather than just one part of it. For example, when considering 300-hPa height anomalies in the mid- to high latitudes of the Northern Hemisphere, an anomaly high

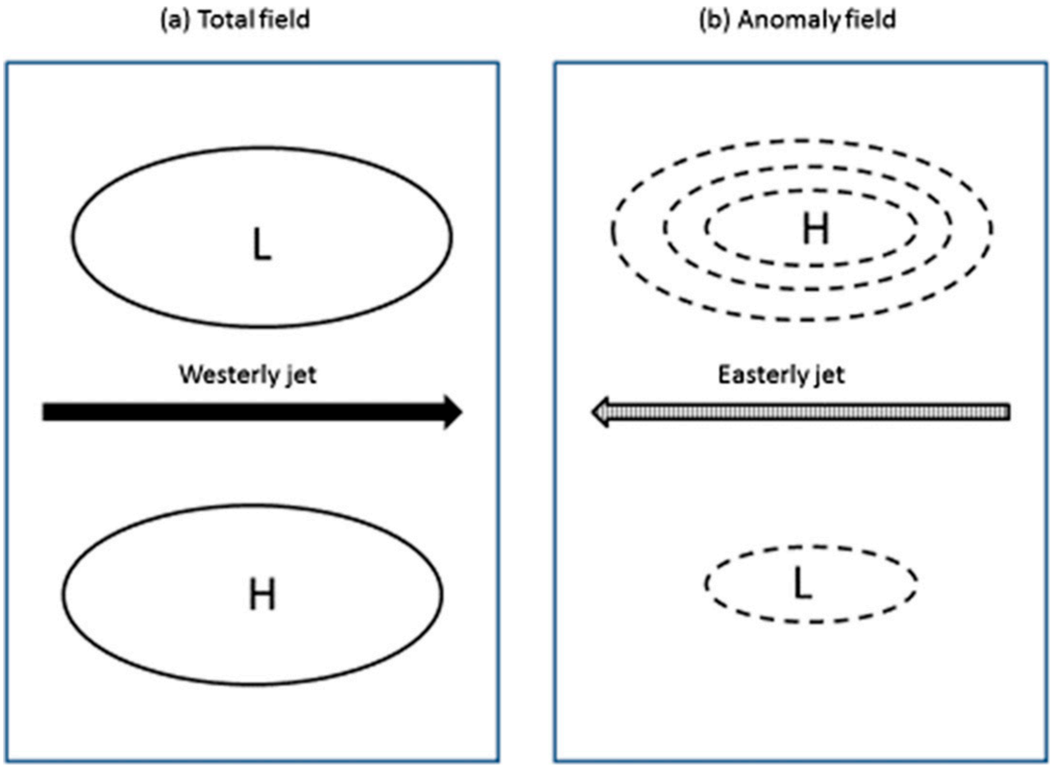

FIG. 2. A schematic comparison between (a) total height/wind and (b) anomalous height/wind at the 300-hPa level in the Northern Hemisphere (H = high, L = low).

north of an anomaly low translates into a weakening of the westerly jet (Fig. 2a) rather than a presence of an easterly jet (Fig. 2b). On other hand, the anomaly can help to immediately pinpoint the possible cause of the weakening of the westerly jet, that is, whether it is due to the increase of pressure in the north or the decrease of pressure in the south or both, which cannot be easily told by the total field. In this illustration, it is caused mainly by the increase of pressure (weakening of the low system) in the north (Fig. 2b). Land–sea breezes could be another example, if the climatological pattern is an easterly onshore flow due to warm land in the west and cold water in the east. But for some reason, the anomaly pattern is opposite (i.e., a westerly offshore flow). We cannot simply say that there is a land breeze by just viewing the anomalies since in fact the total pattern is completely zeroed out so there is no flow at all in reality. The weather phenomenon along this coastline should be associated with the total calm flow rather than the anomalous westerly flow. Thus, just considering the anomaly pattern would be misleading. However, by viewing the spatial scale and structure of anomaly patterns in wind and temperature, one might quickly tell the cause of this abnormality. For example, is it due to abnormally warmer water temperature or colder than normal land temperature or stronger large-scale westerly flow? Therefore, we suggest that the anomaly approach should be used as a supplemental tool to a total field to mitigate any misuse of an anomaly field. In this study, we will avoid dynamic explanation but focus on the demonstration of the new way of expression (i.e., pattern recognition). If there is any indication of dynamical implication in the description of our results below, it is not our intention.

Using a heavy rain situation as an example, this paper is intended to systematically examine the pros and cons of employing anomaly fields compared to total fields in weather analysis (weather forecasting is not a concern in this paper). The paper is organized as follows. Section 2 describes the data and methodology. Results are presented in section 3, where basic atmospheric variables (height, temperature, wind, and humidity) are examined first and diagnostic parameters (divergence, vorticity, potential vorticity, and their variations) are examined separately in the following two subsections. A summary and discussion are provided in section 4.

2. Data and methodology

a. Datasets

Two datasets are used in this paper. The first one is the observed daily 24-h (1200–1200 UTC) accumulated precipitation of 754 rain gauges in mainland China during the period 1991–98. The gauges are dense and evenly

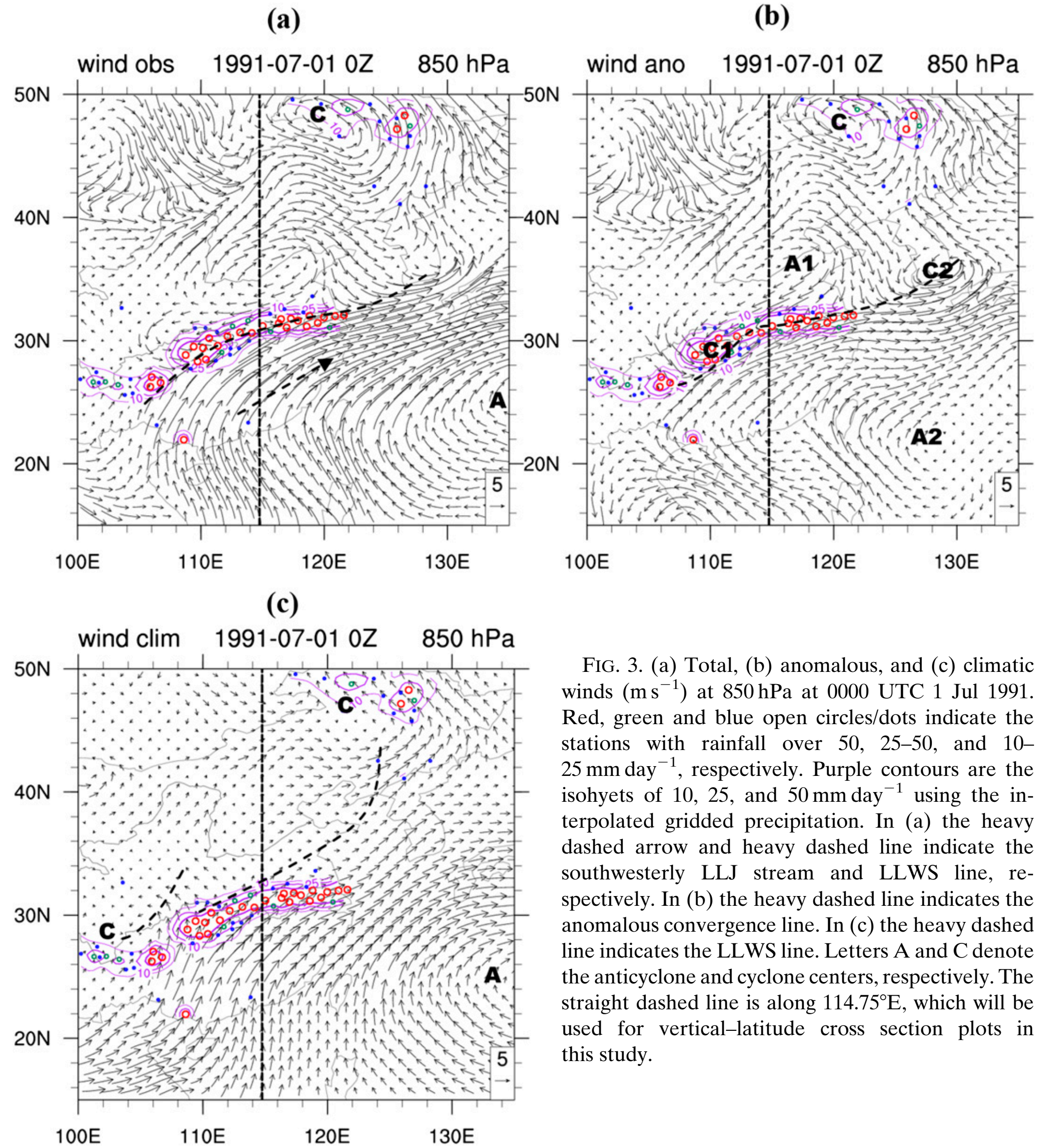

FIG. 3. (a) Total, (b) anomalous, and (c) climatic winds ($\mathrm{m\,s^{-1}}$) at 850 hPa at 0000 UTC 1 Jul 1991. Red, green and blue open circles/dots indicate the stations with rainfall over 50, 25–50, and 10–25 mm $\mathrm{day^{-1}}$, respectively. Purple contours are the isohyets of 10, 25, and 50 mm $\mathrm{day^{-1}}$ using the interpolated gridded precipitation. In (a) the heavy dashed arrow and heavy dashed line indicate the southwesterly LLJ stream and LLWS line, respectively. In (b) the heavy dashed line indicates the anomalous convergence line. In (c) the heavy dashed line indicates the LLWS line. Letters A and C denote the anticyclone and cyclone centers, respectively. The straight dashed line is along 114.75°E, which will be used for vertical–latitude cross section plots in this study.

distributed in space in eastern China. The siphon rainfall recorder is used in these gauges. Quality control is performed over the database on the criteria of outliers, homogeneity, and consistency. Details can be found in Feng et al. (2004) for the homogeneity and consistency, and in Chen et al. (2010) for the outliers. A daily local heavy rain (LHR) event is defined as when the rainfall accumulated over the 24-h period exceeds 50 mm. A daily regional heavy rain (RHR) event is determined as two or more adjacent stations (less than 200 km apart) reaching 50 mm within 24 h. The term heavy rain is referred to as a daily RHR event in this study. This observed precipitation dataset is interpolated onto a 0.5° × 0.5° latitude–longitude grid using the ordinary Kriging method of Chen et al. (2010), and is used for quantitative calculation of various measuring scores. The second dataset is the ECMWF interim reanalysis (ERA-Interim) dataset (http://apps.ecmwf.int/datasets/data/interim-full-daily/) with 0.75° × 0.75° latitude–longitude grid spacing and 37 standard pressure levels (1000–50 hPa) since 1979 (the modern satellite era). The ERA-Interim dataset from 1981 to 2010 was used in the estimation of the climatology, while the 1991 and 1998 datasets were used for the case studies.

b. Method

A total atmospheric variable $F_{d,y}(\lambda, \varphi, p, t)$ can be decomposed into a climatic component $\tilde{F}_d(\lambda, \varphi, p, t)$ and an anomaly $F'_{d,y}(\lambda, \varphi, p, t)$ (Qian et al. 2014):

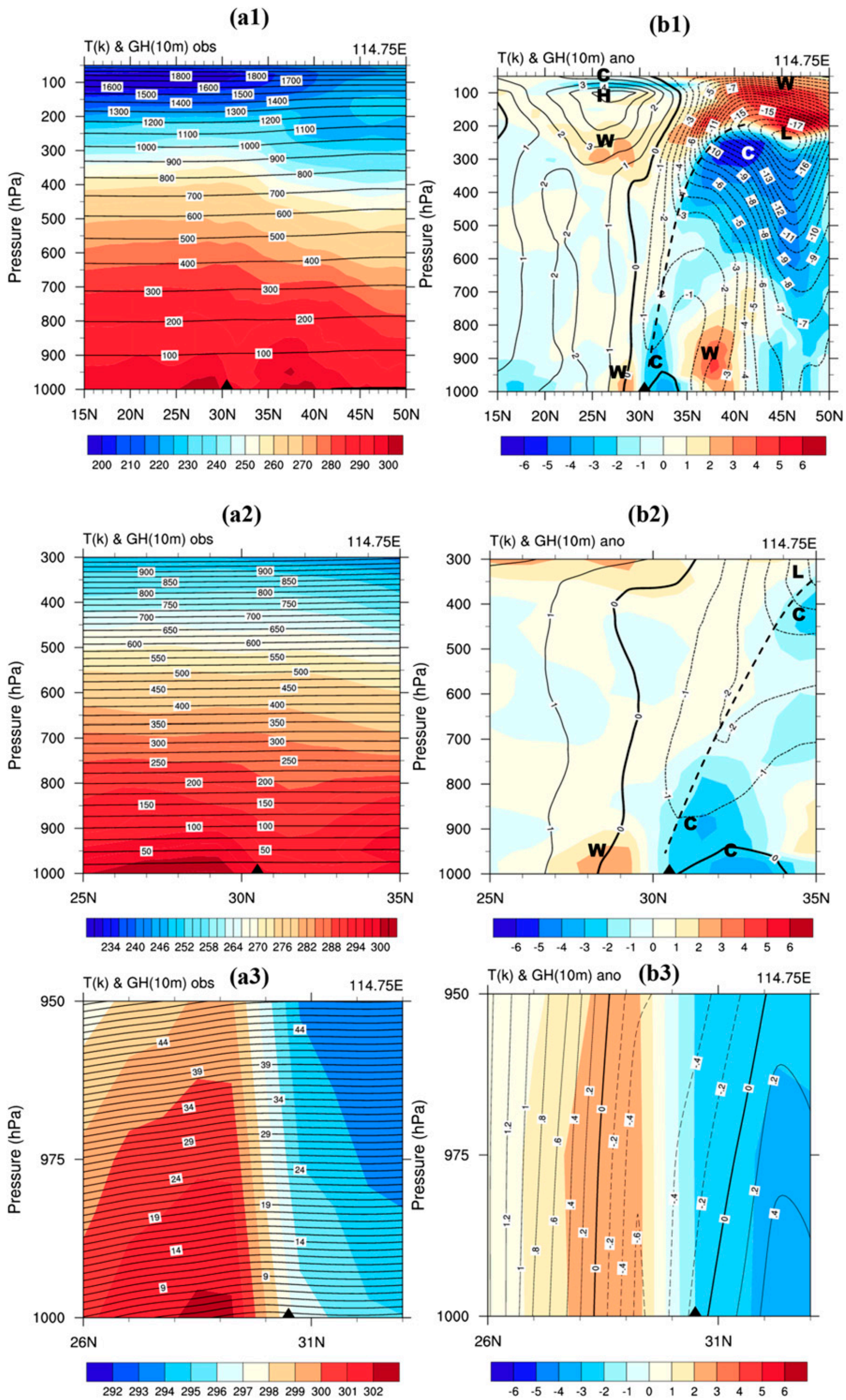

FIG. 4. Vertical–latitude cross sections of (a1)–(a3) total and (b1)–(b3) anomalous height and temperature in hemispheric, regional, and local scales, along 114.75°E at 0000 UTC 1 Jul 1991. Contours are for height or the height anomaly, and color shading is for temperature or the temperature anomaly. The heavy dashed line denotes the axis of the height anomalies in (b1) and (b2). The location of the surface rainband is indicated by the filled triangle. Different contour intervals are used for different scales: In (a1) a 100 × 10 gpm interval is used for height and a 5-K interval for temperature; in (b1) a 1 × 10 gpm interval is used for the height anomaly and a 1-K interval for the temperature anomaly. In (a2) 25 × 10 gpm and 2 K are used; in (b2) 1 × 10 gpm and 1 K are used. In (a3) 1 × 10 gpm and 1 K are used; in (b3) 0.2 × 10 gpm and 1 K are used. Letters H/L and W/C indicate the centers of the height and temperature anomalies, respectively.

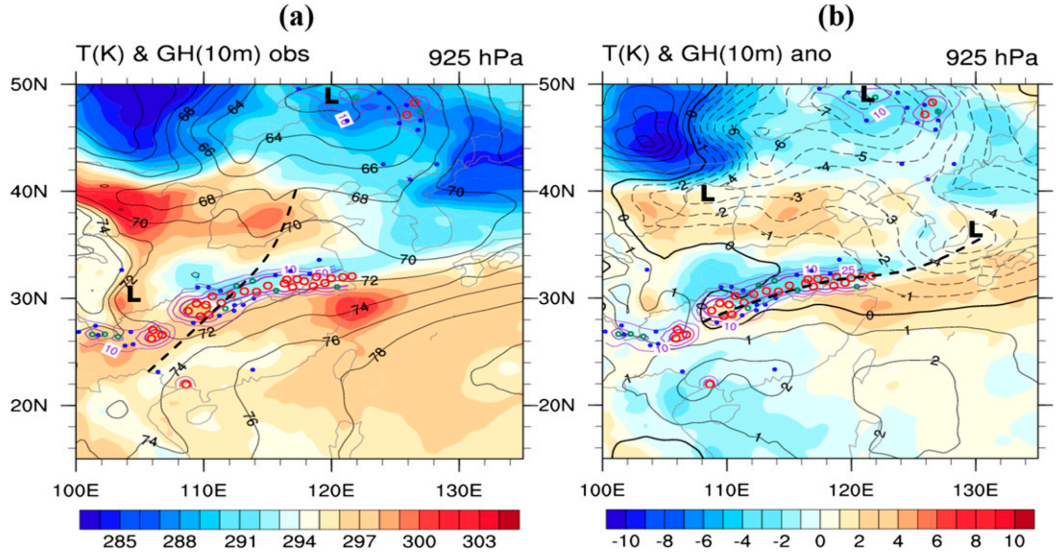

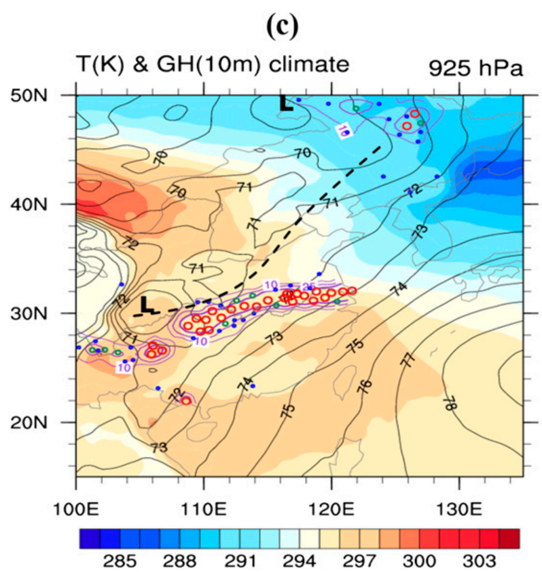

FIG. 5. (a) Total, (b) anomalous, and (c) climatic height and temperature at 925 hPa at 0000 UTC 1 Jul 1991. The red, green, and blue open circles/dots indicate the stations with rainfall exceeding 50, 25–50, and 10–25 mm day^{-1}, respectively. In (a) and (c) the contours are for height (10-gpm interval) and color shading is for temperature (1-K interval). In (b) contours are for height anomalies (10-gpm interval) and shading is for temperature anomalies (1-K interval). The heavy dashed line denotes the height trough. Purple contours are the isohyets of 10, 15, and 50 mm day^{-1} using the interpolated gridded precipitation.

$$F_{d,y}(\lambda, \varphi, p, t) = \tilde{F}_d(\lambda, \varphi, p, t) + F'_{d,y}(\lambda, \varphi, p, t), \qquad (1)$$

where t is the diurnal time (24 h day^{-1}), d is the calendar date (365 days yr^{-1}), y is the year, φ is the latitude, λ is the longitude, and p is the pressure level. The climatic field is estimated by averaging 30 yr (1981–2010) of data based on the reanalysis dataset for a date d and a time t:

$$\tilde{F}_d(\lambda, \varphi, p, t) = \sum_{y=1981}^{2010} F_{d,y}(\lambda, \varphi, p, t)/30. \qquad (2)$$

It is assumed that the positive and negative anomalies of meteorological variables at a specific grid point and a given time roughly cancel each other during the 30-yr period to approximate the quasi-static climatic state. The climate defined by Eq. (2) varies from hour to hour and from day to day. To obtain a smoother hour-to-hour climatology, two other separate methods, the four mode of Fourier expansion and the 21-day running mean, were individually applied at NCEP (B. Yang 2013, personal communication). We have compared these three methods and found that the differences in the mean among them are much smaller than the variance at four selected times (not shown), which implies that using any one of them as the "standard" climatology should lead to the same conclusion although minor differences in the climatological values are expected. Equations (1) and (2) are therefore used to obtain the climatology and anomaly of the geopotential height H, temperature T, specific humidity q, and wind $\mathbf{v} = u\mathbf{i} + v\mathbf{j} + \omega\mathbf{p}$ based on the ERA-Interim reanalysis data in this study.

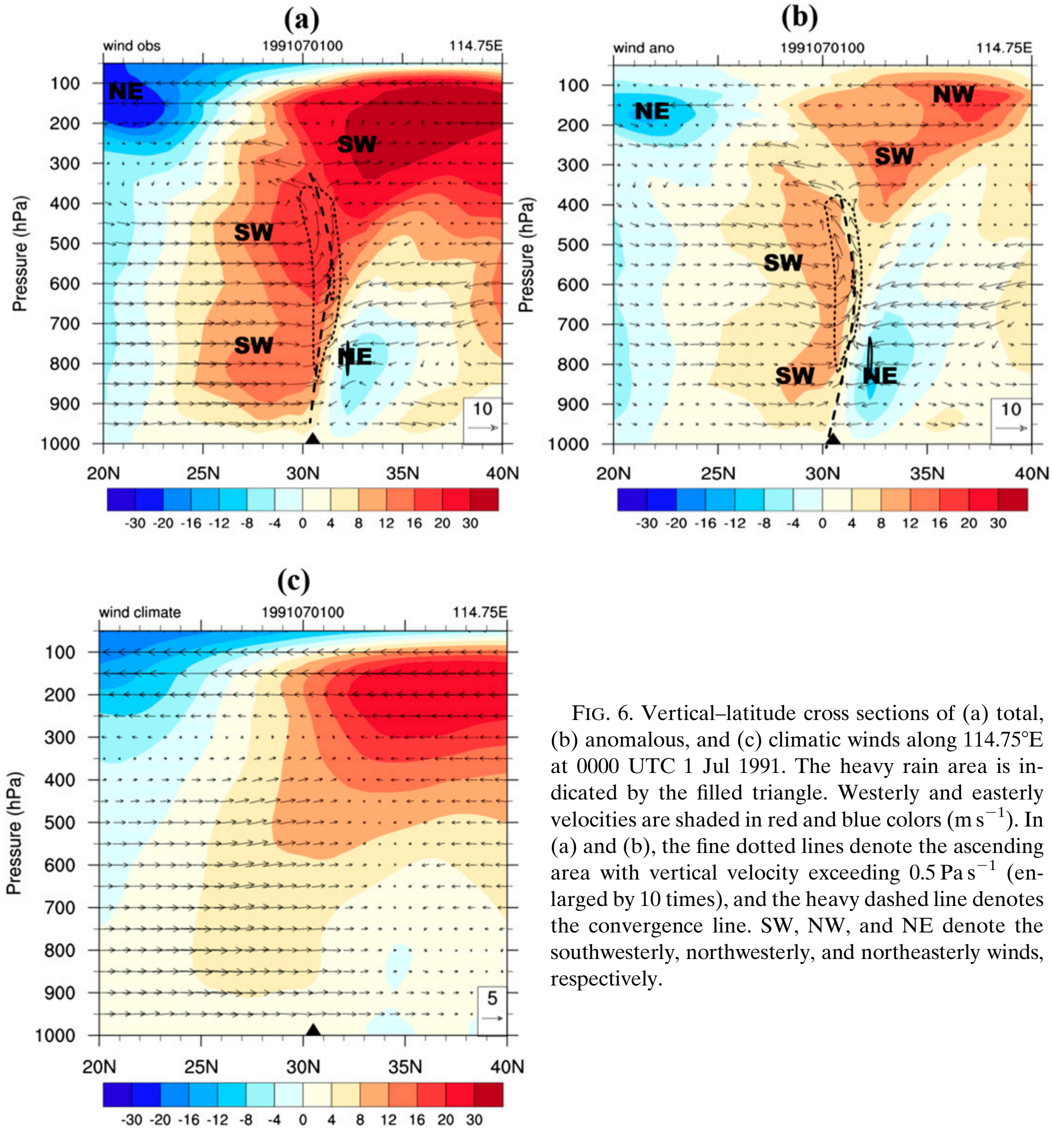

FIG. 6. Vertical–latitude cross sections of (a) total, (b) anomalous, and (c) climatic winds along 114.75°E at 0000 UTC 1 Jul 1991. The heavy rain area is indicated by the filled triangle. Westerly and easterly velocities are shaded in red and blue colors (m s^{-1}). In (a) and (b), the fine dotted lines denote the ascending area with vertical velocity exceeding 0.5 Pa s^{-1} (enlarged by 10 times), and the heavy dashed line denotes the convergence line. SW, NW, and NE denote the southwesterly, northwesterly, and northeasterly winds, respectively.

3. Comparison between total and anomalous fields

a. Basic atmospheric variables

From 30 June to 12 July 1991, a prolonged stationary flood-producing precipitation event occurred over the lower Yangtze River basin, in response to a series of short waves moving east across the area (Ding 1993). On 1 July 1991, 22 stations exceeded 50 mm day^{-1} of rainfall with a maximum precipitation of 201.8 mm day^{-1} and an average precipitation of 96.5 mm day^{-1}. Figure 3 shows the total, anomalous, and climatic winds at 850 hPa at 0000 UTC 1 July 1991. In the total wind field (Fig. 3a), a heavy rainband is located on the left side of the low-level jet (LLJ) and near the horizontal low-level wind shear (LLWS) line, where the southwesterly flow is much stronger on the south side of the shear line; there is no visible presence of cyclonic systems associated with this rainband. By contrast, two synoptic-scale cyclonic vortices, one over the upper Yangtze River valley (labeled C1) and another over South Korea (C2), are clearly observed in the anomaly wind field (Fig. 3b), which are connected by an anomalous wind shear line along the Yangtze River. Two anticyclone centers (A1 and A2) are situated on each side of the anomalous wind convergence line over the lower Yellow River and the subtropical northwest Pacific, respectively. The anomalous convergence line overlaps with the heavy rainband. Although the LLWS lines in both the total and anomaly fields indicated the rainband location equally well, the anomalous lows and highs can only be revealed in the anomaly wind field. The LLWS lines in the climatic wind are apparently not a good

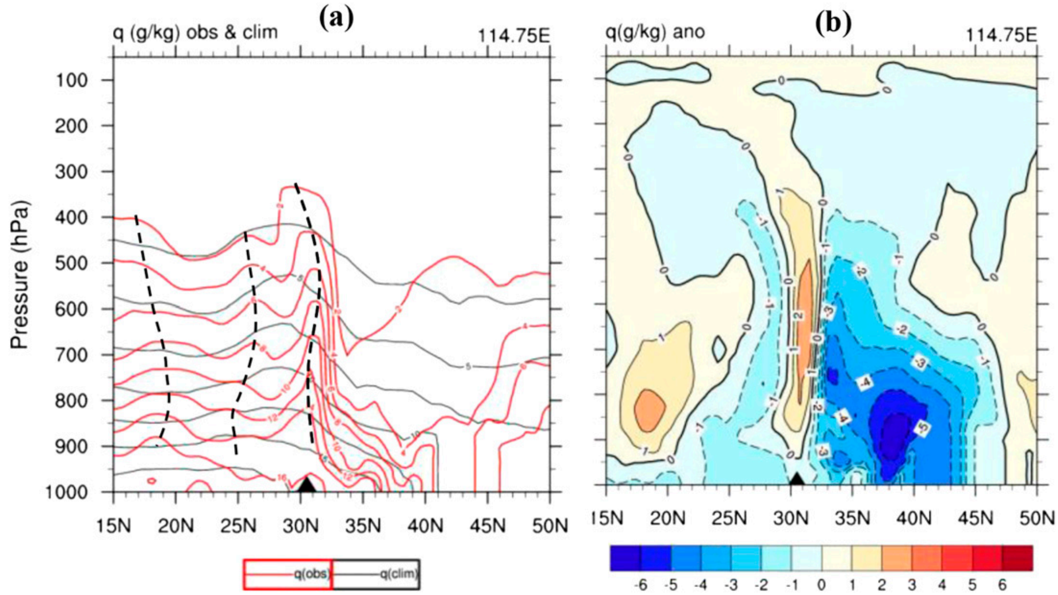

FIG. 7. Vertical–latitude cross sections of q along 114.75°E at 0000 UTC 1 Jul 1991. (a) Total q (red line in 2 g kg^{-1} interval), as well as its climatic component (black dashed line, 2.5 g kg^{-1} interval). (b) The q anomaly (shaded with 1 g kg^{-1} contour interval). The thick dashed lines in (a) represent the axes of maximum total specific humidity.

indicator for the heavy rainband (Fig. 3c), as one would expect.

Figure 4 compares the vertical–latitude cross sections of the total and anomalous height-temperature distributions, along 114.75°E (corresponding to the straight vertical dashed line in Fig. 3) at 0000 UTC 1 July 1991. To have a complete comparison, three different scales (hemispheric, regional, and local) are provided. At all three scales, both the total and anomalous temperature fields have an equally visible signal (a frontal zone with a large temperature contrast) connecting to the heavy rain event. However, there is no obvious signal that allows for identification of the rainband from the total height distribution in hemispheric and regional scales as a result of the small difference in geopotential height across the heavy rain area (Figs. 4a1 and 4a2). At the local scale, the heavy rain was located in a height ridge area in the total field (Fig. 4a3) because it is climatologically a subtropical-high area (not shown). By contrast, the height anomalies show a clear signal indicating the rainband, where an axis of negative height anomalies is extended down and southward from the upper troposphere to the heavy rain area in all scales (Figs. 4b1–3). These features indicate that vertical coupling between the lower- and upper-troposphere atmospheric systems might have played a role in the formation of this heavy rain event. Apparently, this vertical coupling information cannot be easily seen from the total height field. This demonstrates that some small but important features are hard to see or may be obscured in the presence of the climatological background in a total field but can be vividly revealed after the climatology part is removed. This is an added value of the anomaly approach to the total-field-based analysis.

Since both the height and temperature anomalies have clear signals in the lower troposphere as shown in Fig. 4b, the horizontal distributions of the total, anomalous, and climatic height–temperature distributions at 925 hPa at 0000 UTC 1 July 1991 are compared in Fig. 5. As in Fig. 4, both the total and anomalous temperature fields have similar capability to indicate the heavy rain; that is, a large temperature gradient zone lies along the rainband. In the 925-hPa height field, the north boundary of the heavy rainband is better defined by the narrow anomaly trough (Fig. 5b), while it is located on the north edge of a large total-height gradient zone (Fig. 5a). Therefore, the rainband width, especially its north boundary, looks to be more easily defined by the narrow anomaly trough than by the wide pressure-uniform area in the total height field. In the climatic field (Fig. 5c) there is no well-defined signal indicating the rainband, as expected. Figure 5b also shows an extension of the anomaly trough across southern South Korea with an anomaly low center. Although the dataset utilized in this study did not contain rainfall records outside of China, the South Korean observations confirmed that a regional heavy rain event did occur over southern South Korea in response to this anomaly vortex.

The total and anomalous winds in the vertical–latitude cross sections along 114.75°E at 0000 UTC 1 July 1991

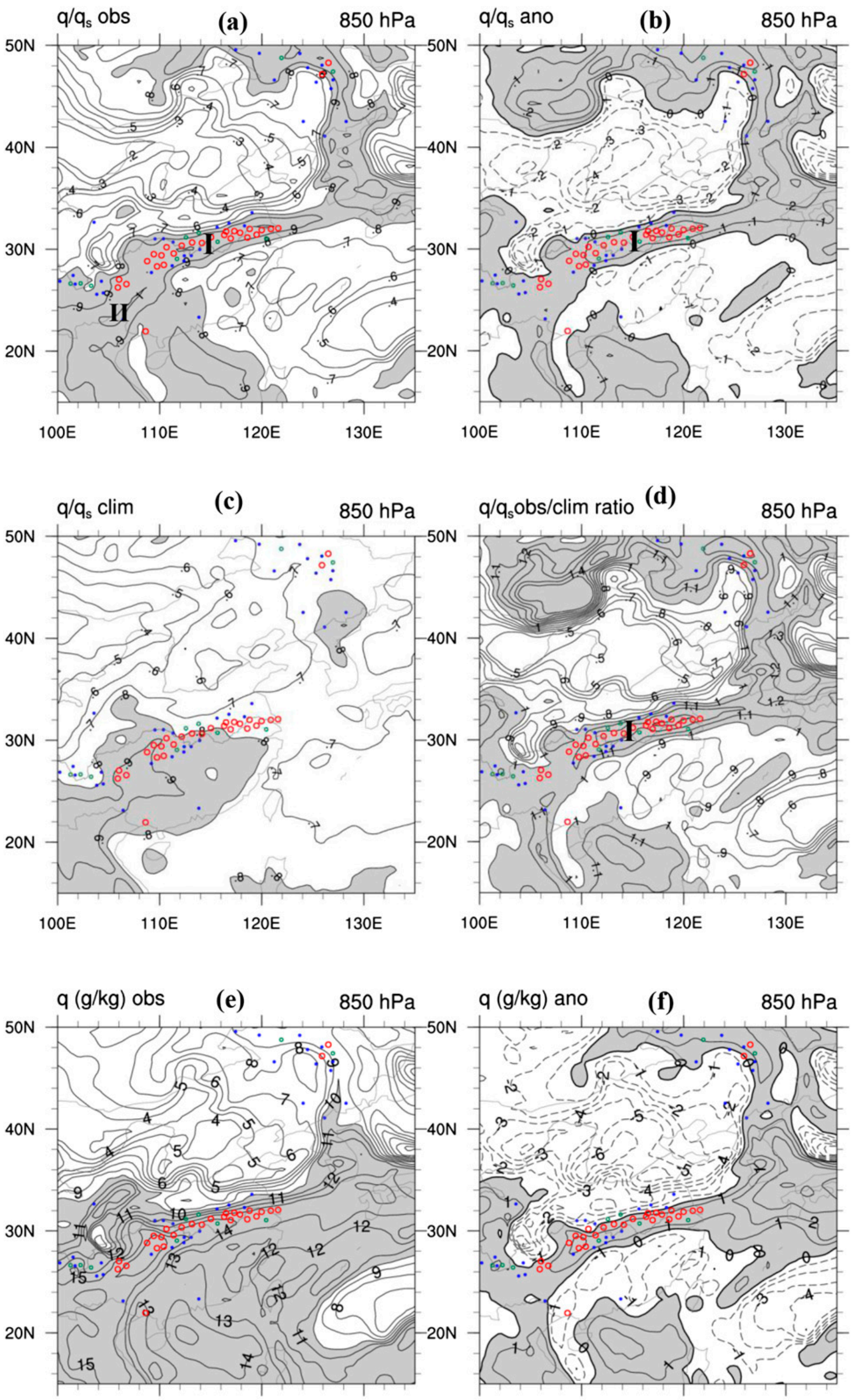

FIG. 8. Horizontal distributions of (a) total, (b) anomalous, and (c) climatic RH (q/q_s) at 850 hPa at 0000 UTC 1 Jul 1991, in 0.1 or 10% contour intervals. (d) The ratio of the total RH to the climatic RH, at 0.1 contour intervals. (e) Total and (f) anomalous q, in 1 g kg^{-1} contour intervals. Red, green, and blue open circles/dots indicate the stations with rainfall over 50, 25–50, and 10–25 mm day^{-1}, respectively.

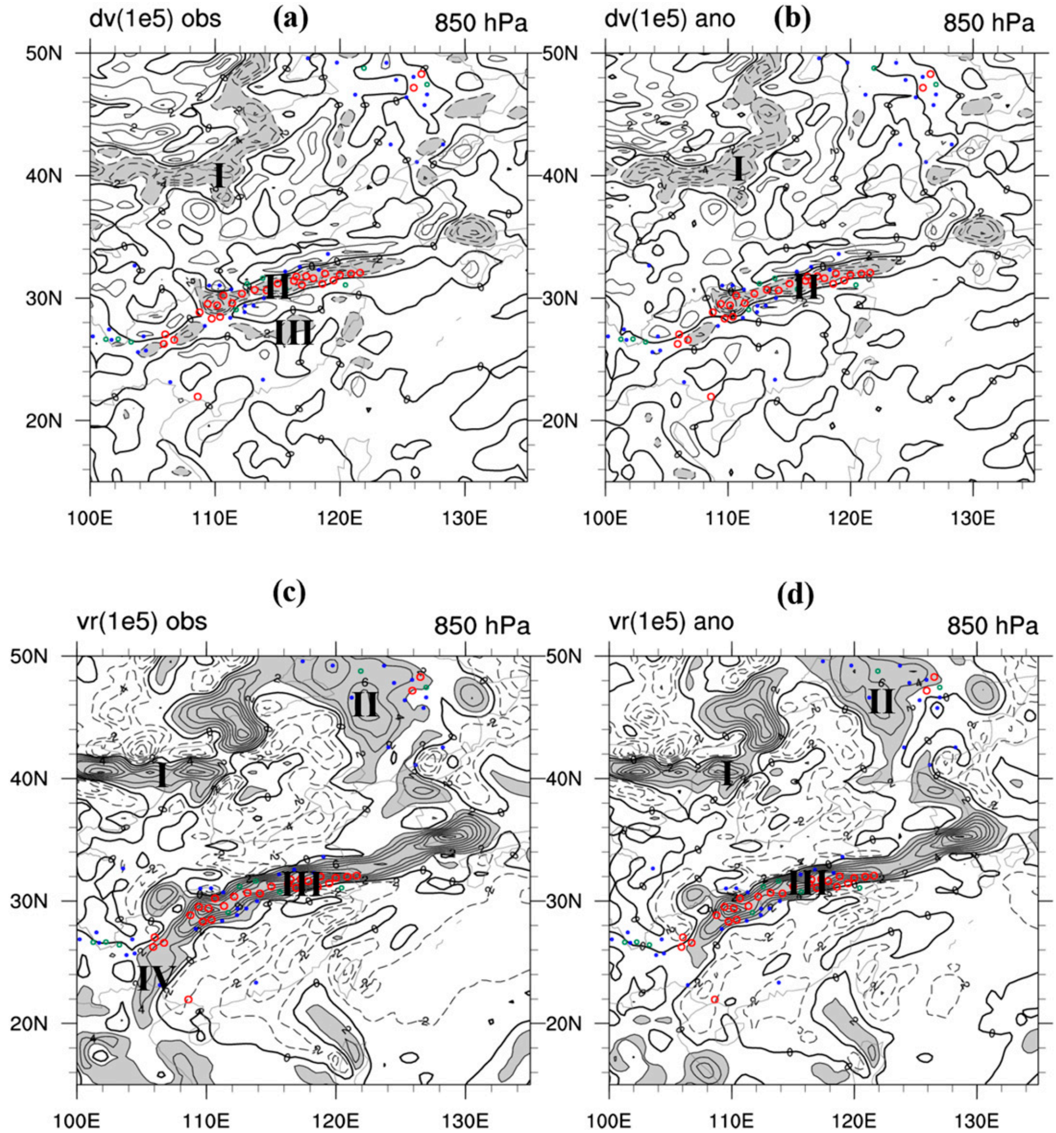

FIG. 9. (a) Total and (b) anomalous divergence; (c) total and (d) anomalous relative vorticity at 850 hPa at 0000 UTC 1 Jul 1991. Contour interval is $2 \times 10^{-5}\,\mathrm{s}^{-1}$. Convergence bands or positive voriticy bands are denoted by I–IV. The areas of divergence (vorticity) lower than $-2 \times 10^{-5}\,\mathrm{s}^{-1}$ (greater than $2 \times 10^{-5}\,\mathrm{s}^{-1}$) are shaded. Red, green, and blue open circles/dots indicate the stations with rainfall over 50, 25–50, and 10–25 mm day^{-1}, respectively.

are compared in Fig. 6. The convergence of the winds and ascending motion are evident in the mid- to low troposphere over the heavy rain area in both the total (Fig. 6a) and anomalous (Fig. 6b) winds. However, the contrast between southwesterly (SW) and northeasterly (NE) is clearer and more concentrated in the anomaly field, particularly between 950 and 400 hPa, because of the reduced SW and the enhanced NE after the climatology (Fig. 6c) is removed. This is consistent with the results from Fig. 3. Besides the deeper depth of the low-level convergence, the convergence zone in the anomaly field is vertically more tilted and shifted more to the south near the surface.

The advantage of an anomaly-based over a total-field-based approach is also noticeable in the moisture field. Both specific humidity q and relative humidity (RH) q/q_s are examined. In the vertical distribution of q, both the total (Fig. 7a) and anomaly (Fig. 7b) fields do show an axis of maximum value directly above the heavy rain area. But the structure is more visible and well organized in the anomaly field: the axis of the positive moisture anomaly is accompanied by a negative moisture anomaly on both the north and south sides. Because of the climatologically high value (the black contours in Fig. 7a), the distribution of q is almost opposite in the

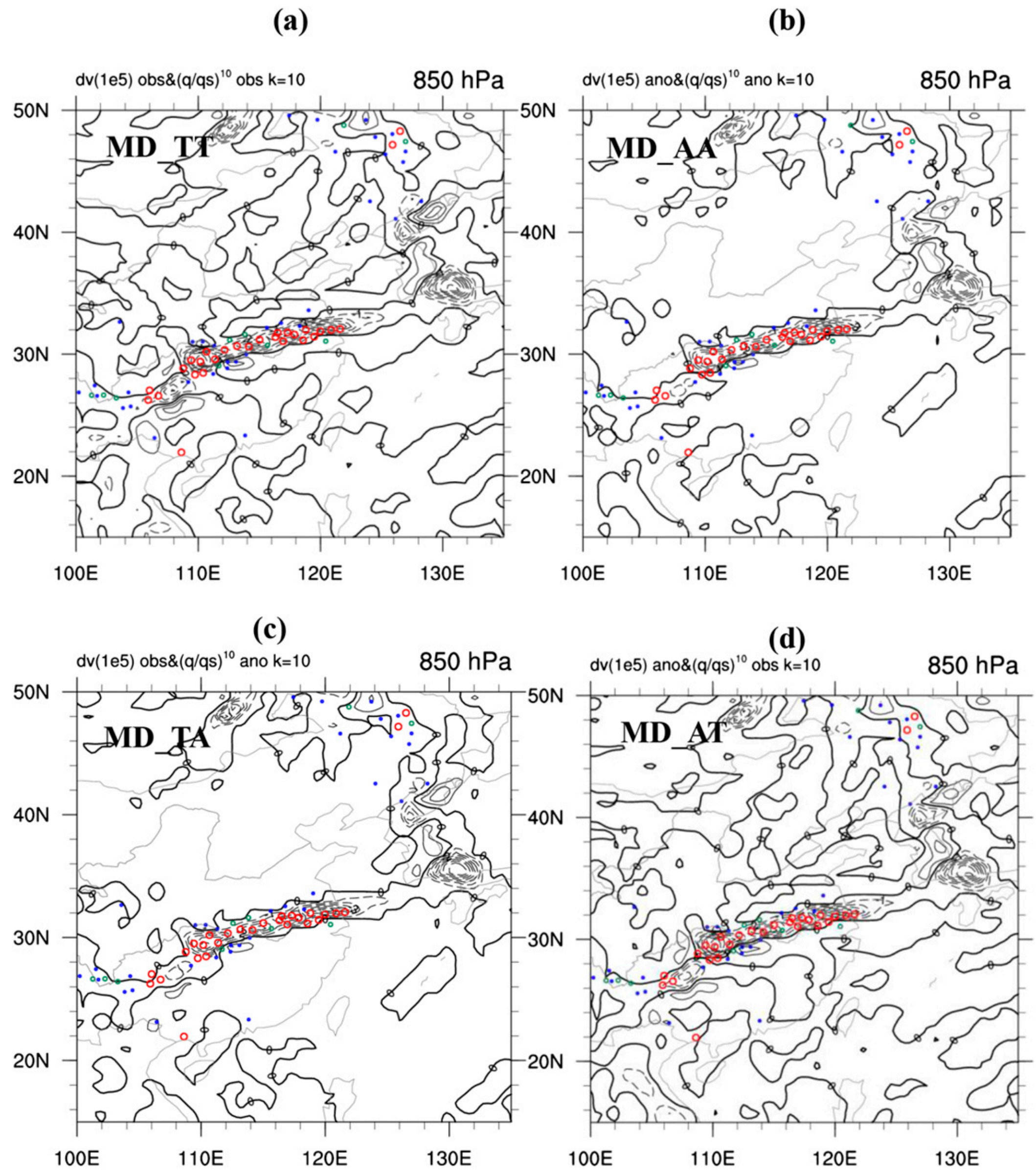

FIG. 10. MD at 850 hPa at 0000 UTC 1 Jul 1991. (a) MD_TT, (b) MD_AA, (c) MD_TA, and (d) MD_AT. The contour interval is $1 \times 10^{-5}\,s^{-1}$ and $k = 10$ is used in the calculations. Red, green, and blue open circles/dots indicate the stations with rainfall over 50, 25–50, and 10–25 mm day^{-1}, respectively.

total and anomaly fields near 25°N, with a moisture ridge in the total field but a moisture trough in the anomaly field. In the horizontal distribution of RH, both the total (Fig. 8a) and anomaly (Fig. 8b) fields do have a high RH belt that covers the Yangtze River heavy rainband. However, the high RH belt in the total field covers a much wider area extending from Vietnam all the way to the Yangtze River via southwest China (area II + I in Fig. 8a). The RH within this area is almost uniform (with a maximum in the nonheavy rain area II) and indistinguishably covers both the heavy rain and nonheavy rain regions. In contrast, the anomalous RH shows a maxima zone that is concentrated mainly in the heavy rain area (area I in Fig. 8b). This certainly provides a more meaningful signal to forecasters. The reason why the false-alarm area II is absent in the anomaly field is that Vietnam and southwest China are climatologically wetter than the Yangtze River valley (Fig. 8c). After the climate background is removed, what is revealed is an anomaly signal that has a closer relation with daily weather anomalies. This anomaly signal is even clearer if it is expressed by the ratio of the total RH to the climatic

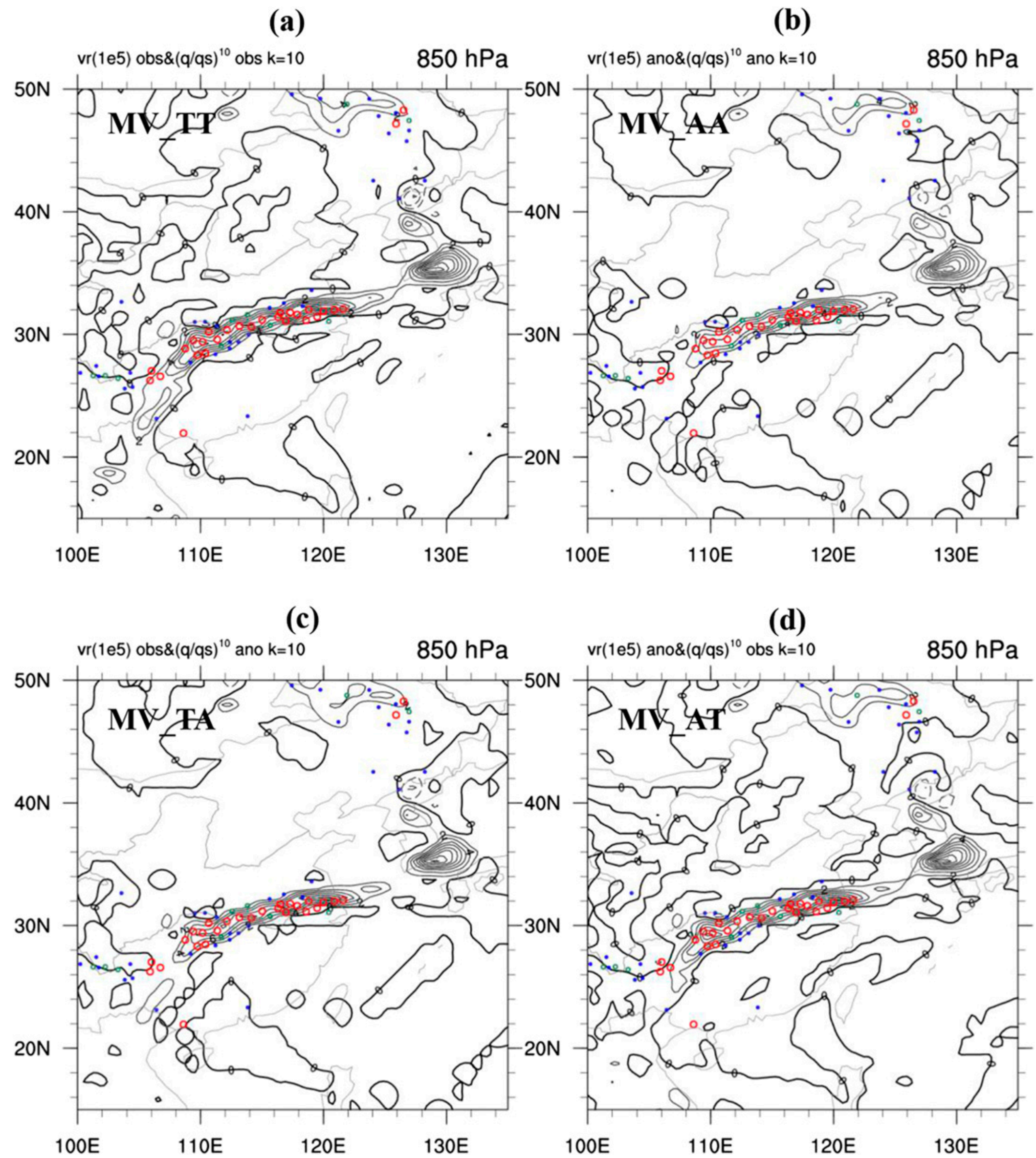

FIG. 11. As in Fig. 10, but for MV with $k = 10$. The contour interval is $2 \times 10^{-5}\,\mathrm{s}^{-1}$.

RH (Fig. 8d). The climatic component mainly reflects the large-scale wet southwest Asian monsoon and dry air mass in the northwest China desert region, which has little correlation with the heavy rain event. The horizontal distribution of specific humidity field is generally similar to that of the relative humidity in both the total (cf. Figs. 8e and 8a) and anomalous (cf. Figs. 8f and 8b) components. The heavy rainband is collocated with a maximum band of positive specific humidity anomalies. One advantage of using q instead of RH exists in the climatologically dry region, that is, the anomalously wet zone in terms of RH is now replaced by an anomalously dry zone in terms of q in the northwest corner where no rain was observed. This positive RH anomaly was likely caused by the abnormally lower temperature (as indicated by Fig. 5b) rather than by excessive moisture content. Note that since dynamical factors are not considered, not all areas with anomalously high moisture are expected to have heavy rain events (the impact of combining moisture and dynamical factors together has been investigated in detail in Qian et al. 2015).

Figures 3–8 demonstrated that anomaly-based weather analysis has advantages over the total-field-based approach. Generally speaking, the anomalies have a more concentrated signal (pattern) near the heavy rainband

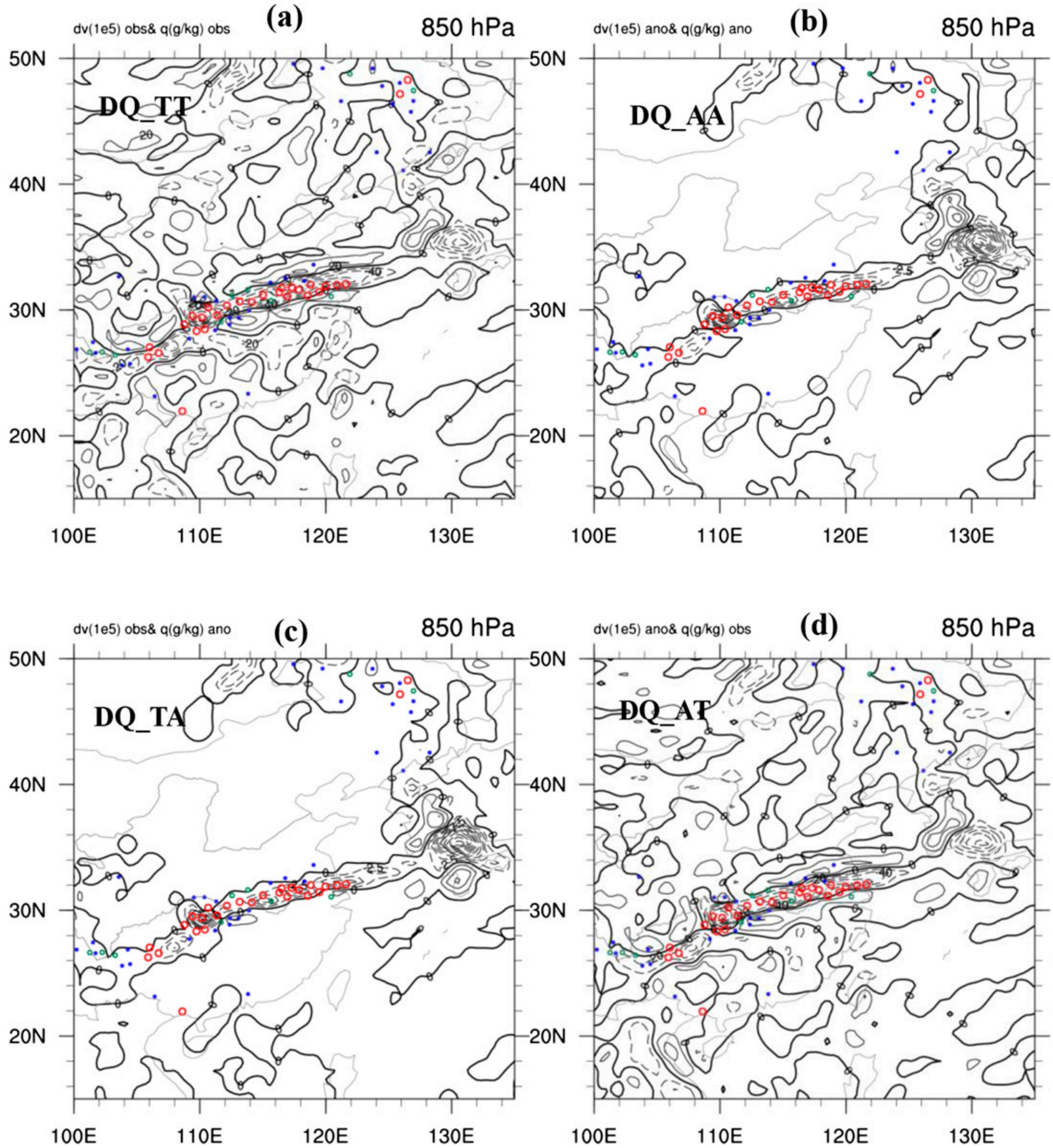

FIG. 12. As in Fig. 10, but for DQ. The contour intervals are $20 \times 10^{-5}\,\mathrm{s}^{-1}\,\mathrm{g\,kg}^{-1}$ in (a) and (d) and $2.5 \times 10^{-5}\,\mathrm{s}^{-1}\,\mathrm{g\,kg}^{-1}$ in (b) and (c).

leading to an easier identification of anomalous episodes. Although the total fields also have a positive indication of the rainband, the anomaly fields provide more detailed anomalous structures. Therefore, the anomaly-based weather analysis can be a valuable supplement to the current total-field weather analysis to give forecasters a more complete picture of a weather event. Examination of numerous other heavy rain events (including those that occurred during the period of 30 June–12 July 1991 as well as another 41 cases from 1998 that were used in sections 3b and 3c) supported the results found in this case study. In addition to heavy rain (Qian et al. 2013), similar results have been found for other weather events such as freezing rain, heat waves, summer low temperatures, and typhoon tracks (Qian and Zhang 2012; Ding and Qian 2012; Qian et al. 2014; Qian and Jiang 2014; Qian et al. 2016; Huang et al. 2015). Therefore, we are confident that the above result with respect to basic atmospheric variables is representative and can be generalized.

b. Nonconservative thermodynamic parameters

In this section, a few nonconservative thermodynamic parameters including divergence, relative vorticity, moist divergence (MD), moist vorticity (MV), specific humidity q, and the two products of divergence and

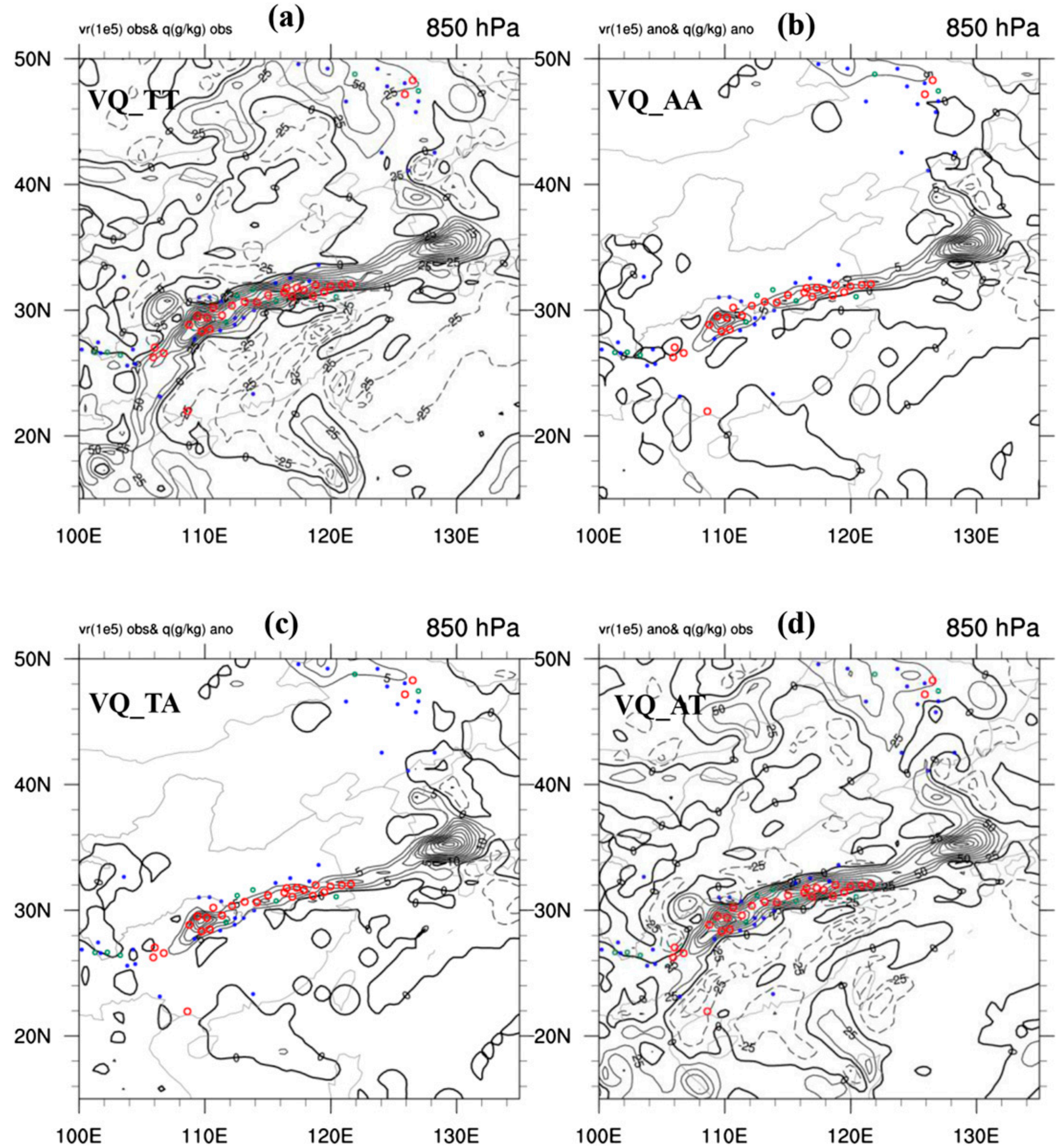

FIG. 13. As in Fig. 10, but for VQ. The contour intervals are $25 \times 10^{-5}\,\mathrm{s^{-1}\,g\,kg^{-1}}$ in (a) and (d) and $5 \times 10^{-5}\,\mathrm{s^{-1}\,g\,kg^{-1}}$in (b) and (c).

vorticity directly multiplying by q (DQ and VQ) will be examined. These are given by

$$D = \left(\frac{\partial u}{\partial x} + \frac{\partial v}{\partial y}\right), \tag{3}$$

$$\zeta = \left(\frac{\partial v}{\partial x} - \frac{\partial u}{\partial y}\right), \tag{4}$$

$$\mathrm{MD} = \left(\frac{\partial u}{\partial x} + \frac{\partial v}{\partial y}\right) \cdot \left(\frac{q}{q_s}\right)^k, \tag{5}$$

$$\mathrm{MV} = \left(\frac{\partial v}{\partial x} - \frac{\partial u}{\partial y}\right) \cdot \left(\frac{q}{q_s}\right)^k, \tag{6}$$

$$\mathrm{DQ} = \left(\frac{\partial u}{\partial x} + \frac{\partial v}{\partial y}\right) \cdot q, \quad \text{and} \tag{7}$$

$$\mathrm{VQ} = \left(\frac{\partial v}{\partial x} - \frac{\partial u}{\partial y}\right) \cdot q, \tag{8}$$

where $k = 10$ is used in the MD and MV following Qian et al. (2015). For details about the concept of MD and MV, readers are referred to Qian et al. (2015). By applying Eq. (1) to the zonal and meridional wind components u and v, the divergence and vorticity can be expressed in total, climatic, and anomalous components, that is, $D = (\partial u/\partial x) + (\partial v/\partial y)$, $\tilde{D} = (\partial \tilde{u}/\partial x) + (\partial \tilde{v}/\partial y)$, and $D' = (\partial u'/\partial x) + (\partial v'/\partial y)$ for divergence; and

TABLE 1. Averaged TS, POD, areal bias, and FAR of MPV and specific humidity q at 850 hPa, GMPV at 925 hPa, as well as various forms of divergence and vorticity at 850 hPa in depicting heavy rain locations ($\geq$25 mm day^{-1}) based on 41 cases that occurred in eastern China in 1998. The optimal thresholds used for each parameter are listed.

Parameter		POD	Bias	FAR	TS	Optimal threshold
Divergence (850 hPa; s^{-1})	Div	0.295	1.12	0.707	0.169	-2.0×10^{-5}
	Div′	0.355	1.60	0.757	0.167	-1.4×10^{-5}
Moist divergence (850 hPa; $k = 10$; s^{-1})	MD_TT (div $\times q/q_s$)	0.488	1.37	0.612	0.270	-0.5×10^{-5}
	MD_TA (div $\times q'/q_s'$)	0.449	1.22	0.592	0.263	-0.5×10^{-5}
	MD_AT (div′ $\times q/q_s$)	0.476	1.33	0.610	0.268	-0.5×10^{-5}
	MD_AA (div′ $\times q'/q_s'$)	0.441	1.23	0.603	0.257	-0.4×10^{-5}
Vorticity (850 hPa; s^{-1})	Vort	0.357	1.27	0.694	0.196	4.3×10^{-5}
	Vort′	0.403	1.51	0.711	0.201	3.4×10^{-5}
Moist vorticity (850 hPa; $k = 10$; s^{-1})	MV_TT (vort $\times q/q_s$)	0.538	1.749	0.656	0.262	1.4×10^{-5}
	MV_TA (vort $\times q'/q_s'$)	0.561	1.846	0.658	0.266	0.9×10^{-5}
	MV_AT (vort′ $\times q/q_s$)	0.511	1.507	0.619	0.274	1.5×10^{-5}
	MV_AA (vort′ $\times q'/q_s'$)	0.534	1.700	0.646	0.267	0.9×10^{-5}
MPV (850 hPa; PVU)	MPV	0.330	4.992	0.926	0.064	0.03
	MPV1	0.239	1.467	0.824	0.111	0.2
	MPV2	0.280	1.316	0.777	0.131	−0.2
	MPV′	0.322	4.286	0.915	0.007	0.05
	MPV1′	0.244	1.572	0.834	0.109	0.2
	MPV2′	0.249	1.311	0.814	0.116	−0.1
GMPV (925 hPa; $k = 10$; PVU)	GMPV	0.420	1.748	0.739	0.188	0.4
	GMPV1	0.315	1.935	0.822	0.129	0.2
	GMPV2	0.343	1.720	0.774	0.154	0.2
	GMPV′	0.464	2.043	0.756	0.189	0.3
	GMPV1′	0.326	2.080	0.827	0.127	0.2
	GMPV2′	0.316	1.827	0.811	0.132	0.1
Specific humidity (850 hPa; g kg^{-1})	q	0.674	3.902	0.734	0.179	12.9
	q'	0.582	2.915	0.758	0.192	2.3
DQ (850 hPa; s^{-1} g kg^{-1})	DQ_TT (div $\times q$)	0.349	0.962	0.631	0.219	-21.8×10^{-5}
	DQ_TA (div $\times q'$)	0.419	1.300	0.637	0.228	-2.9×10^{-5}
	DQ_AT (div′ $\times q$)	0.369	1.088	0.648	0.219	-17.3×10^{-5}
	DQ_AA (div′ $\times q'$)	0.441	1.500	0.671	0.222	-2.1×10^{-5}
VQ (850 hPa; s^{-1} g kg^{-1})	VQ_TT (vort $\times q$)	0.434	1.333	0.659	0.231	45.2×10^{-5}
	VQ_TA (vort $\times q'$)	0.469	1.562	0.656	0.240	6.79×10^{-5}
	VQ_AT (vort′ $\times q$)	0.458	1.302	0.636	0.250	38.4×10^{-5}
	VQ_AA (vort′ $\times q'$)	0.528	1.863	0.679	0.244	4.7×10^{-5}

$\zeta = (\partial v/\partial x) + (\partial u/\partial y)$, $\tilde{\zeta} = (\partial \tilde{v}/\partial x) + (\partial \tilde{u}/\partial y)$, and $\zeta' = (\partial v'/\partial x) + (\partial u'/\partial y)$ for vorticity.

Figures 9a and 9b compare the total-wind- and anomaly-wind-based divergences at 850 hPa at 0000 UTC 1 July 1991. Generally speaking, the results are quite similar to each other. In the total-field-based divergence, there are three bands of convergence located, respectively, over north China (I), the Yangtze River valley (II), and south China (III), where only the one along the Yangtze River is associated with heavy rain (Fig. 9a). The convergence band in south China, however, is largely reduced in the anomalous divergence (Fig. 9b) because it is caused by the climatic wind (not shown). Therefore, the anomalous divergence has a slightly better indication of heavy rain than the total divergence. As for the strong convergence band in north China revealed in the anomalous divergence field, it did not produce heavy rain because of the lack of atmospheric moisture (see Fig. 8).

Figures 9c and 9d compare the total-wind- and anomaly-wind-based vorticities at 850 hPa at 0000 UTC 1 July 1991. There are a total of four bands of positive vorticity located over north China, northeast China, the Yangtze River valley, and southwest China (IV). As with divergence, the anomalous vorticity is generally similar to the total vorticity in the larger picture with only two differences: one is the elimination of the southwest extension of band IV and the other is a slightly southward shift of the same band (III) in the anomalous vorticity as a result of the removal of the climatic component. The elimination of the southwest extension (IV) can be deemed to be an improvement, while the southward shift is too small to have a meaningful impact in this case. The fact that the positive vorticity band in north China does not correspond to any heavy rain is again due to the lack of atmospheric moisture over that region (see Fig. 8).

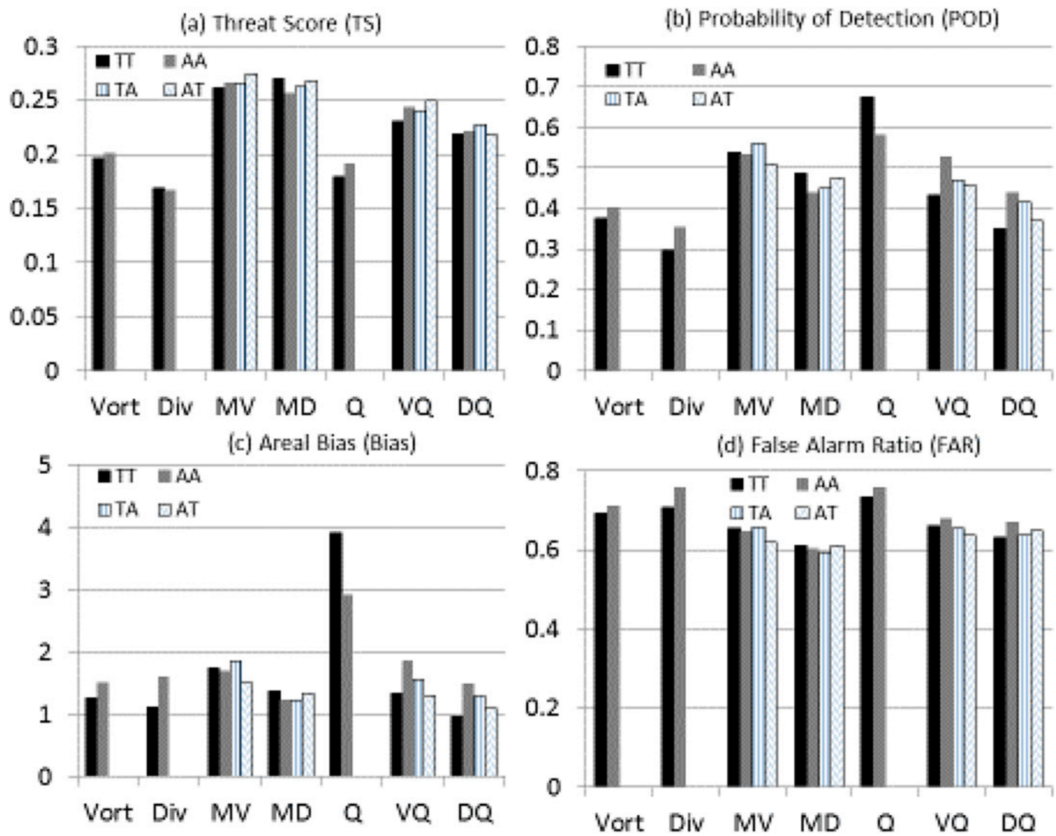

FIG. 14. Average (a) TS, (b) POD, (c) areal bias, and (d) FAR of various vorticity and divergence forms as well as specific humidity (total field shown by black bar, with anomaly versions in gray and other lighter colors) in depicting the heavy precipitation area ($\geq$25 mm day^{-1}) based on a total of 41 daily heavy rain cases that occurred in eastern China during 1998.

The MD and MV are evaluated in four forms: purely total-field based (using total wind and total moisture, denoted as *_TT), purely anomaly-field based (anomalous wind and anomalous moisture, *_AA), and two hybrid versions of mixed total- and anomaly-field based (total wind and anomalous moisture, *_TA; anomalous wind and total moisture, *_AT), where * can be replaced by either MD or MV. Figure 10 shows the four forms of MD at 850 hPa, where the heavy rainband is generally collocated with the strongest convergence zone for all four forms. Although the four versions are similar in general, the two with total moisture (MD_TT and MD_AT) have a stronger convergence zone and are better than the two with anomalous moisture (MD_TA and MD_AA). For example, MD_TT and MD_AT cover the southwest tail of the heavy rainband better than MD_TA and MD_AA. A very similar result is found for the MV at 850 hPa (Fig. 11). The heavy rain is generally collocated with the maximum positive vorticity zone in all four forms: MV_TT (Fig. 11a) and MV_AT (Fig. 11d) are similar to each other and have a stronger signal; MV_TA (Fig. 11c) and MV_AA (Fig. 11b) are similar to each other with a weaker signal. Although MV_AT and MV_TT are generally similar, the former looks slightly better than the latter because the climatologically induced "false alarm" tail in southwest China is gone in MV_AT (cf. Figs. 11a and 11d). This implies that under some circumstances, the mixing of the total and anomaly fields might have the best coverage with the heavy rain area than either using the purely total-field- or purely anomaly-field-based methods for a compound parameter.

As for the MD and MV, the DQ and VQ are examined in the same four forms (*_TT, *_AA, *_TA and *_AT, where * can be replaced by either DQ or VQ). In the two forms (*_AA and *_TA) that involve anomalous q, only positive q' is applied in the calculation (i.e., negative q' is treated as zero) since heavy rain is our concern. The results for DQ and VQ are shown in Figs. 12 and 13, respectively. They show that all four of the forms have a band of high value collocated with the heavy rainband. The two forms using anomalous q

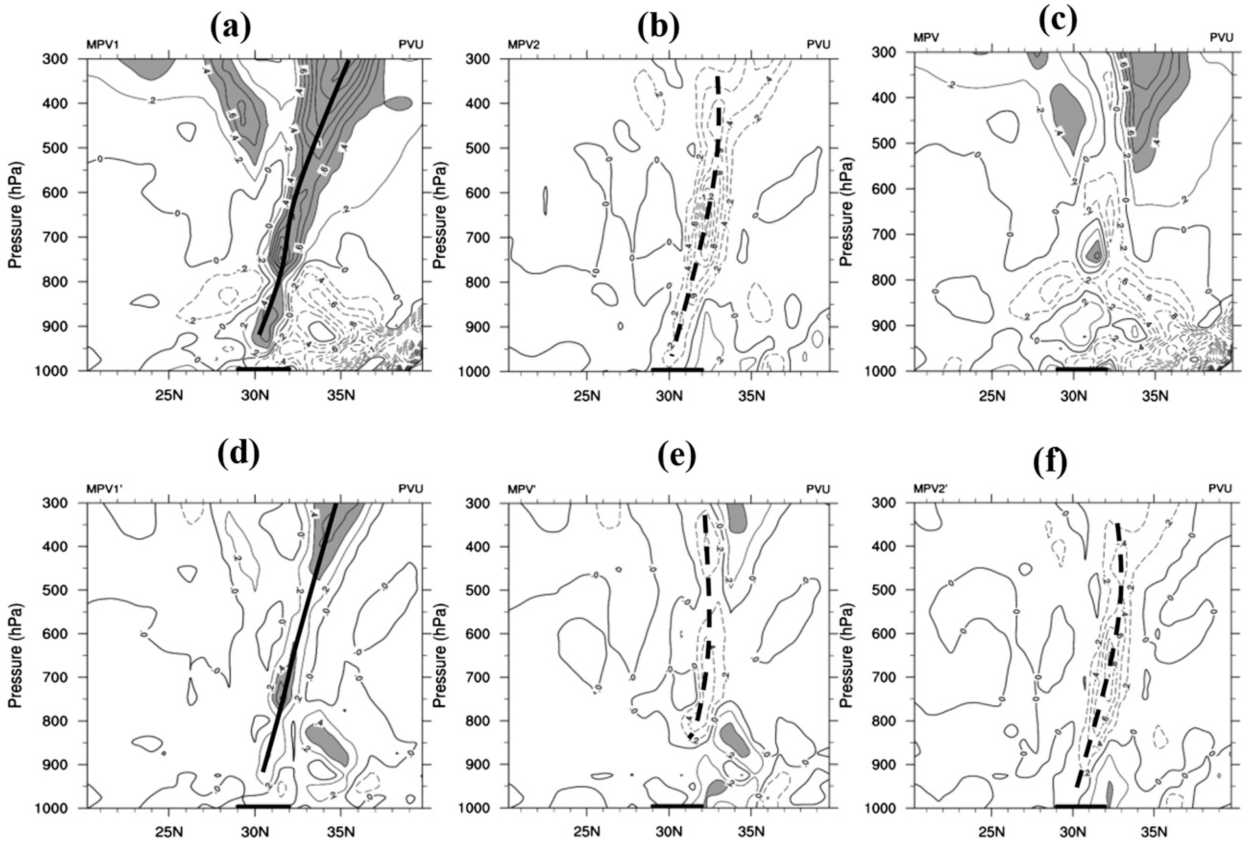

FIG. 15. Vertical–latitude cross sections for (top) total field of (a) MPV1, (b) MPV2, and (c) MPV (the sum of MPV1 and MPV2), as well as (bottom) the anomaly field of (d) MPV1′, (e) MPV2′, and (f) MPV′ (the sum of MPV1′ and MPV2′) along 114.75°E at 0000 UTC 1 Jul 1991. The interval for positive (solid line) and negative (dashed line) cases is 0.2 PVU (1 PVU = 10^{-6} K kg^{-1} m^2 s^{-1}). Heavy solid and heavy dashed lines denote the maximum axis of the positive and negative PV. The thick horizontal line at the surface represents the area of heavy rain.

(*_AA and *_TA in Figs. 12b, 12c, 13b, and 13c) have a more concentrated signal singling out the heavy rainband because only positive q' is used in the calculation.

To have a robust and quantitative result, we have systematically examined the other 41 daily heavy rain events that occurred in eastern China during 1998. The threat score (TS; Palmer and Allen 1949) is used to quantitatively measure how well an area defined by a parameter overlaps with a heavy precipitation area of exceeding 25 mm day^{-1} over China. To be fair for each parameter, an optimal threshold value is estimated first for each parameter, which gives the highest TS on average of the 41 cases (Table 1). The TS results are summarized in Fig. 14a, which reiterates the above case study findings. The TSs suggest that the performances are generally similar between the total and anomaly versions for these parameters. The hybrid version of mixed anomaly-wind- and total-moisture-based MV_AT and VQ_AT covers the heavy rain area slightly better than either the purely total-field-based MV_TT and VQ_TT or the purely anomaly-based MV_AA and VQ_AA (but the differences are not statistically significant).

To better understand the performance or TS result, we calculated the probability of detection (POD; Fig. 14b), areal bias (Fig. 14c), and false alarm ratio (FAR; Fig. 14d) for the same optimal thresholds used in TS [the equations of these scores can be found in Zhou and Du (2010)]. From Fig. 14 we can see that when moisture q is used alone to depict the heavy rain area, it is often too wide in its coverage (high bias) and leads to a high false alarm ratio although its probability of detection is high, which results in worse performance or a lower TS. When the dynamic factor (divergence and vorticity) is used alone, it has a higher false alarm ratio and a lower detection rate, which implies that its location does not match the heavy rain area well and leads to a lower TS. When the moisture and dynamics factors are combined (MV, MD, VQ, and DQ), the false alarm ratio is reduced and the probability of detection is

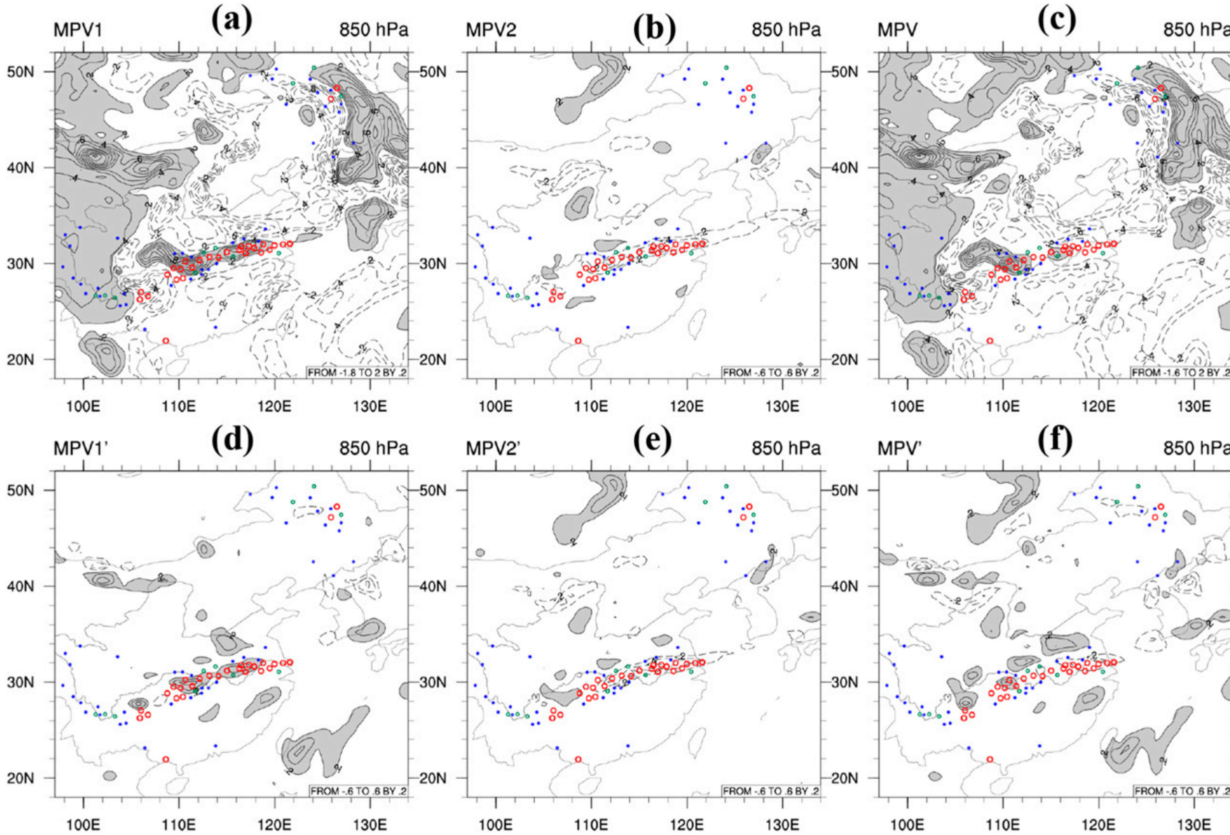

FIG. 16. (top) Total fields of (a) MPV1, (b) MPV2, and (c) MPV, as well as (bottom) anomaly fields of (d) MPV1′, (e) MPV2′, and (f) MPV′ at 850 hPa at 0000 UTC 1 Jul 1991. The interval for positive (solid line) and negative (dashed line) is 0.2 PVU. Red, green, and blue open circles/dots indicate the stations with rainfall over 50, 25–50, and 10–25 mm day^{-1}, respectively.

increased, which results in better performance with a higher TS. The MD and MV are even more superior to the DQ and VQ. Therefore, we recommend combining dynamical and moisture factors together to form a hybrid compound parameter to increase the ability to depict areas of heavy rain, as in Qian et al. (2015).

c. Conservative thermodynamic parameters

For a conservative parameter, it is conservative only in its total field but not in its anomaly field. Therefore, it will be interesting to see how an anomaly field behaves. Two conservative thermodynamic parameters will be examined in this section: moist potential vorticity (MPV) and generalized MPV (GMPV).

$$\mathrm{MPV} = \rho^{-1}\varsigma_a \cdot \nabla\theta_e, \tag{9}$$

where ρ is the air density, $\varsigma_a = f + \varsigma = 2\Omega\sin\varphi + [(\partial v/\partial x) + (\partial u/\partial y)]$ is the absolute vorticity, f is the Coriolis parameter, Ω is the angular speed of the earth's rotation, φ is the earth's geographical latitude, and θ_e is the equivalent potential temperature. The MPV is conservative in moist-adiabatic and frictionless conditions (Schubert et al. 2001) and can be decomposed into two terms:

$$\mathrm{MPV1} = -g(\varsigma + f)\frac{\partial\theta_e}{\partial p} = -g\left[\left(\frac{\partial v}{\partial x} - \frac{\partial u}{\partial y}\right) + f\right]\frac{\partial\theta_e}{\partial p} \tag{9a}$$

and

$$\mathrm{MPV2} = g\left(\frac{\partial v}{\partial p}\cdot\frac{\partial\theta_e}{\partial x} - \frac{\partial u}{\partial p}\cdot\frac{\partial\theta_e}{\partial y}\right). \tag{9b}$$

When the equivalent potential temperature in Eq. (9) is replaced by the generalized equivalent potential temperature, $\theta^* = \theta\cdot\exp[(Lq_s/c_pT)(q/q_s)^k]$, the MPV becomes the GMPV (Gao et al. 2004a):

$$\mathrm{GMPV} = \rho^{-1}\varsigma_a \cdot \nabla\theta^*, \tag{10}$$

where L is latent heat released from condensation by a unit air mass, c_p is the heat capacity of dry air held at a constant pressure, q is air specific humidity, q_s is air saturated specific humidity, and T is air temperature. In GMPV, $k = 10$ is used following Qian et al. (2015).

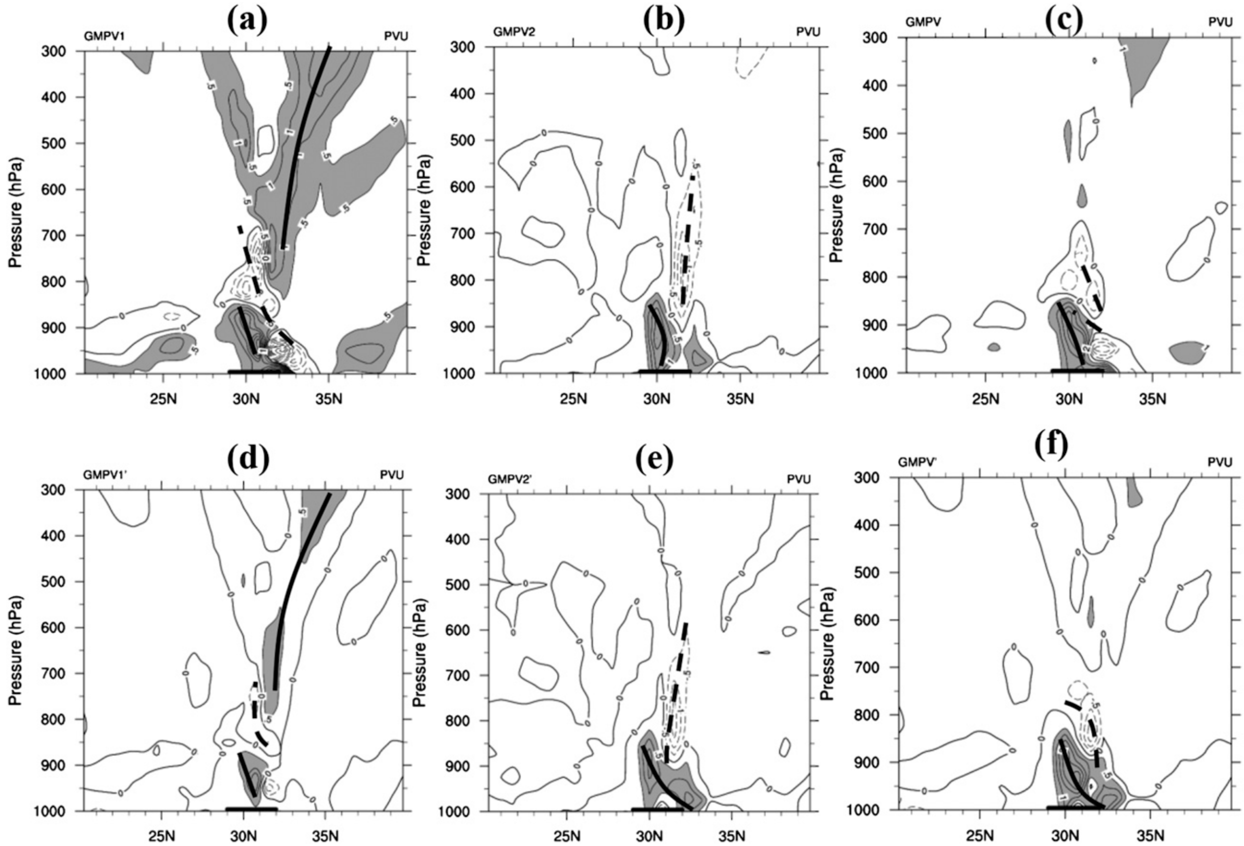

FIG. 17. As in Fig. 15, but for GMPV: (a) GMPV1, (b) GMPV2, (c) GMPV (the sum of GMPV1 and GMPV2), (d) GMPV1′, (e) GMPV2′, and (f) GMPV′ (the sum of GMPV1′ and GMPV2′), using $k = 10$. The interval for positive (solid line) and negative (dashed line) is 0.5 PVU.

Similar to MPV1 and MPV2, GMPV1 and GMPV2 can be defined as

$$\mathrm{GMPV1} = -g(\varsigma + f)\frac{\partial\theta^*}{\partial p} = -g\left[\left(\frac{\partial v}{\partial x} - \frac{\partial u}{\partial y}\right) + f\right]\frac{\partial\theta^*}{\partial p} \quad \text{and} \tag{10a}$$

$$\mathrm{GMPV2} = g\left(\frac{\partial v}{\partial p}\cdot\frac{\partial\theta^*}{\partial x} - \frac{\partial u}{\partial p}\cdot\frac{\partial\theta^*}{\partial y}\right). \tag{10b}$$

Gao et al. (2004a,b) argued that maximum MPV (GMPV) and maximum surface rainfall are nearly collocated as a result of the impact of heat and mass forcing on the development of MPV (GMPV). Therefore, the MPV (GMPV) can be used to track the propagation of rain systems (e.g., Figs. 1–4 in Gao et al. 2004b). We here compare the MPV or GMPV area with the heavy rain area. Similarly, total MPV (GMPV) can be decomposed into climatic and anomalous components if Eq. (1) is applied to all the involved basic variables. Figure 15 is a comparison between the total and anomalous MPV along with its two components in a vertical–latitude cross section along 114.75°E at 0000 UTC 1 July 1991, which shows no obvious advantage of anomaly-field-based MPV′ over total-field-based MPV. Since the maximum axis of MPV1 and MPV2 at 850 hPa is located right over the heavy rainband (Figs. 15a,b), the horizontal comparison is carried out at the 850-hPa level by Fig. 16. The total field (especially MPV1 and MPV) covers a widespread area, while the anomaly field (MPV1′, MPV2′, and MPV′) covers a smaller area and focuses more on the heavy rain regions.

Figure 17 shows the total-field- and anomaly-field-based GMPV along with its two components in a vertical–latitude cross section. There is no major difference between GMPV and GMPV′ in the distribution. Both show a generally correct signal in the lower troposphere pointing to the heavy rain location. Since the signals from GMPV concentrate in the lower troposphere, Fig. 18 shows a spatial distribution of GMPV at 925 hPa. We can see both the advantages and disadvantages associated with the total-field GMPV and anomaly-field based GMPV. Consistent with Fig. 17, the two components have the same sign and all of them,

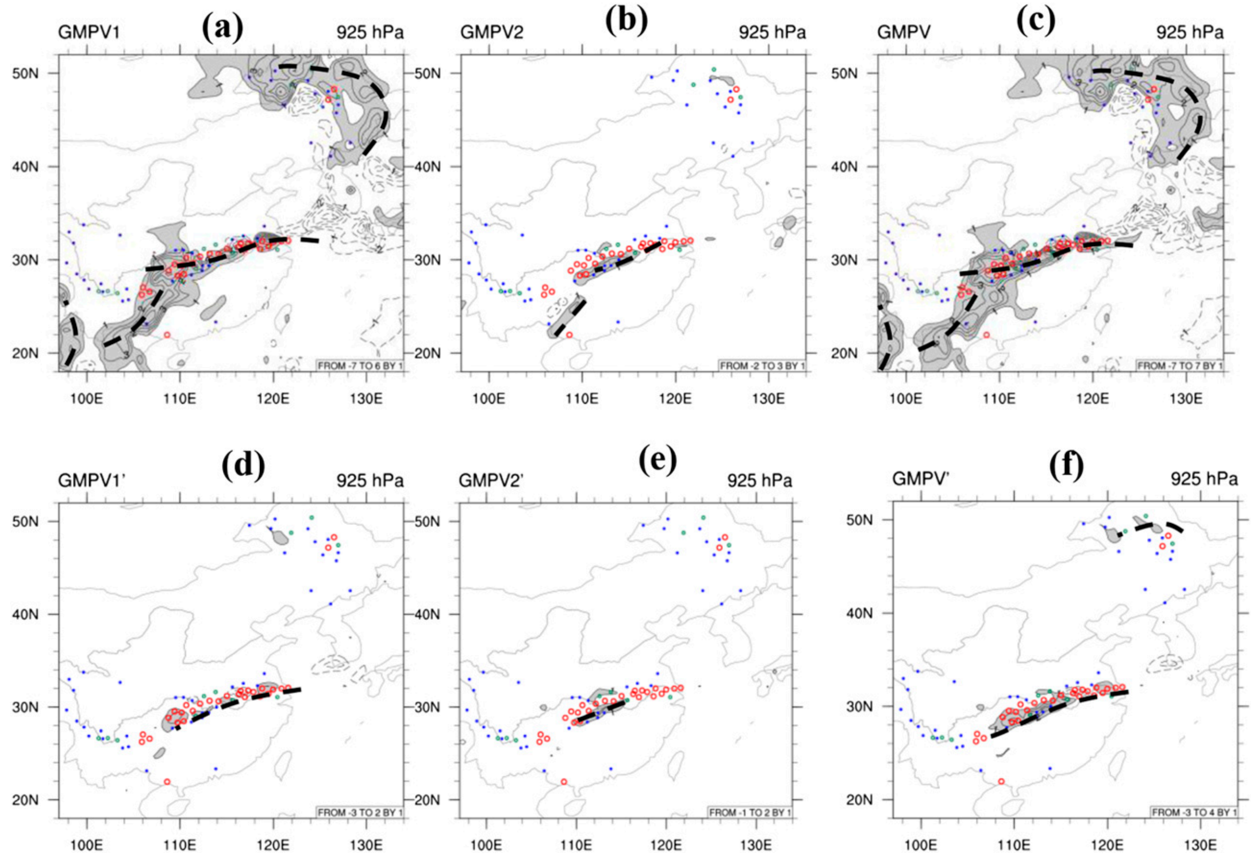

FIG. 18. As in Fig. 16, but for (top) total field of (a) GMPV1, (b) GMPV2, and (c) GMPV, as well as (bottom) anomaly field of (d) GMPV1′, (e) GMPV2′, and (f) GMPV′ at 925 hPa at 0000 UTC 1 Jul 1991. The interval for positive (solid line) and negative (dashed line) is 1.0 PVU. Heavy dashed lines denote the maximum axis of the positive PV.

including their combined term GMPV, more or less cover the heavy rain area. Similar to the MPV, the total GMPV has much wider areal coverage than the anomalous GMPV′. Therefore, GMPV has better coverage but has many false alarms relative to the heavy rain areas, while the GMPV′ signal has a much smaller coverage area resulting in many misses but focuses more directly on the heavy rain regions. Figure 19a shows the averaged TSs based on the 41 cases under each parameter's optimal threshold (also in Table 1). For GMPV, the anomaly-field-based GMPV′ shows similar performance in depicting the heavy rain area when compared to the total-field-based GMPV, while GMPV1′ and GMPV2′ are slightly worse than GMPV1 and GMPV2. For MPV, the MPV′, MPV1′, and MPV2′ results are found to be slightly worse than MPV, MPV1, and MPV2 overall. Since the scales represented in the anomaly field are much more detailed than those in the total field, the TS, which penalizes more for misses than false alarms, probably favors more the total-field approach compared to the anomaly field. Slightly worse TSs for the anomaly field than for the total field might indicate they have similar performance. Probability of detection, areal bias, and false alarm ratio are also calculated for MPV and GMPV. These scores are generally similar between the total and anomaly-based fields (Figs. 19b–d). When one interprets the results between figures and scores, it should keep in mind that the same contour interval was normally used for both the total and anomaly fields in the figures but the scores were calculated based on the optimal threshold of each individual parameter.

4. Conclusions and discussion

Although the use of anomalies in the forecast process (such as an "anomaly forecast") has been shown to be useful and has gradually caught forecasters' attention, current short-range (1–3 days) weather analyses and forecasts are predominantly total-field based. This paper has systematically examined the pros and cons of anomaly-based versus total-field-based approaches in weather analysis using a case study from 1 July 1991 and 41 cases from 1998, to quantify the results, of heavy rain events that occurred in China. The comparison is done

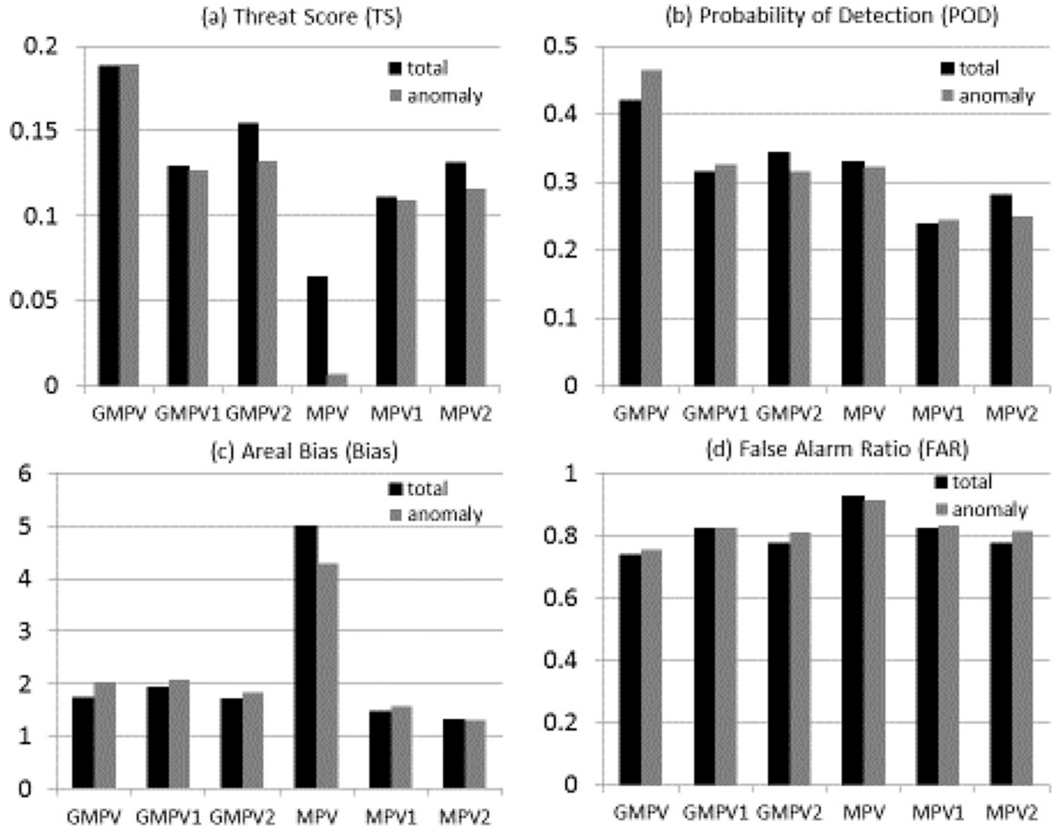

FIG. 19. Average (a) TS, (b) POD, (c) areal bias, and (d) FAR of various MPV and GMPV forms (total field shown by the black bar; anomaly field in gray) in depicting heavy precipitation areas ($\geq$25 mm day^{-1}) based on a total of 41 daily heavy rain cases that occurred in eastern China during 1998.

for both basic atmospheric variables (height, temperature, wind, and humidity) and diagnostic compound parameters (divergence, vorticity, and potential vorticity). Generally, anomaly fields show a more enhanced and concentrated signal (pattern) directly related to high-impact weather events, while total fields can obscure the visualization of anomaly features as a result of the climatic background. This benefit depends, however, on the types of variables. Specifically, the advantage is noticeable for basic atmospheric variables, but is marginal (similar or slightly better) in nonconservative diagnostic parameters, such as divergence and vorticity, and is lost in conservative diagnostic parameters such as potential vorticity. For the conservative parameters MPV and GMPV, the anomaly-field-based results do show advantages over those that are total-field based; that is, the anomaly fields are more focused on heavy rain locations. At the same time, the anomaly fields have disadvantages; that is, they are not able to completely cover heavy rain areas because of the smaller areal coverage. Our results also suggested that under some circumstances, neither total nor anomaly fields (but rather a mix of the two) depicts heavy rain area the best for a compound parameter. Overall, the anomaly-based weather analysis could be a valuable supplement to the conventional total-field-based analysis.

There are limitations as well as benefits when using this anomaly approach. First, this decomposition approach should be considered as an alternative way to present information already contained in the total field rather than providing new information. However, this new method of expression could help forecasters in a meaningful way such as easier identification of anomalous episodes and better visualization of anomalous structures. Since a large deviation from climatology is a strong indicator that anomalous weather events may occur, an anomaly approach can quickly draw a forecaster's attention to what he or she should pay attention to in daily weather forecasting. This could save forecasters time and efforts in a time-restricted operational environment. Second, an anomaly field cannot be used alone (without a total field) to interpret underlying dynamics since any weather phenomenon (such as precipitation) occurs as a result of total flow rather than just anomalous flow alone. At the same time, a spatially or temporally anomalous pattern may immediately pinpoint possible meteorological causes to an abnormal weather event. Therefore, the anomaly and total fields should be used together to maximize the advantages of both approaches.

Our ultimate goal is to use this anomaly approach to decompose model data to improve upon a model's direct forecasts; further work is needed to demonstrate this potential in an operational environment. For example, cases to examine include how model-derived anomalies of other dynamical and moisture variables can improve upon a model's direct precipitation forecasts. As an early attempt, we evaluated a few dynamic-moisture compound diagnostic parameters (MV, MD, VQ and DQ) in the second half of this paper. By comparing Figs. 14 and 19, we can see that the pair (all versions) of MV and MD (~0.26–0.27 in TS) is most capable for indicating regional heavy rain areas followed by the combination of DQ and VQ (~0.22–0.25 in TS). The GMPV group (~0.13–0.19 in TS) has a similar performance level compared to the group of vorticity and divergence (~0.17–0.20 in TS) and the group of q (~0.18–0.19 in TS), while the MPV group is the least capable (~0.01–0.13 in TS). Therefore, the advantage of combining dynamical and moisture factors together to form a hybrid compound parameter is apparent in efforts to increase the ability to depict heavy rain areas.

Acknowledgments. We acknowledge the positive suggestions and encouragements from the all reviewers and editors who have helped us to reach a more balanced view about this work. Ms. Mary Hart of NCEP has helped us to improve the readability of the manuscript. This work is supported by the National Natural Science Foundation of China (41375073) and the Strategic Priority Research Program of the Chinese Academy of Sciences (XDA0509400) and the Key Technologies R&D Program (201306032).

REFERENCES

Chen, D., T. Ou, L. Gong, C. Y. Xu, W. Li, C. H. Ho, and W. H. Qian, 2010: Spatial interpolation of daily precipitation in China: 1951–2005. *Adv. Atmos. Sci.*, **27**, 1221–1232, doi:10.1007/s00376-010-9151-y.

Ding, T., and W. H. Qian, 2012: Statistical characteristics of heat wave precursors in China and model prediction (in Chinese). *Chin. J. Geophys.*, **55**, 1472–1486.

Ding, Y., 1993: *Research on the 1991 Persistent, Severe Flood over Yangtze–Huai River Valley* (in Chinese). Chinese Meteorological Press, 255 pp.

Du, J., R. H. Grumm, and G. Deng, 2014: Ensemble anomaly forecasting approach to predicting extreme weather demonstrated by extremely heavy rain event in Beijing (in Chinese). *Chin. J. Atmos. Sci.*, **38**, 685–699.

Feng, S., Q. Hu, and W. H. Qian, 2004: Quality control of daily meteorological data in China, 1951–2000: A new dataset. *Int. J. Climatol.*, **24**, 853–870, doi:10.1002/joc.1047.

Gao, S. T., X. R. Wang, and Y. S. Zhou, 2004a: Generation of generalized moist potential vorticity in a frictionless and moist adiabatic flow. *Geophys. Res. Lett.*, **31**, L12113, doi:10.1029/2003GL019152.

——, Y. S. Zhou, X. P. Cui, and G. P. Dai, 2004b: Impacts of cloud-induced mass forcing on the development of moist potential vorticity anomaly during torrential rains. *Adv. Atmos. Sci.*, **21**, 923–927, doi:10.1007/BF02915594.

Graham, R. A., and R. H. Grumm, 2010: Utilizing normalized anomalies to assess synoptic-scale weather events in the western United States. *Wea. Forecasting*, **25**, 428–445, doi:10.1175/2009WAF2222273.1.

——, T. Alcott, N. Hosenfeld, and R. H. Grumm, 2013: Anticipating a rare event utilizing forecast anomalies and a situational awareness display: The western U.S. storms of 18–23 January 2010. *Bull. Amer. Meteor. Soc.*, **94**, 1827–1836, doi:10.1175/BAMS-D-11-00181.1.

Grumm, R. H., 2011a: New England record maker rain event of 29-30 March 2010. *Electron. J. Oper. Meteor.*, **12** (4). [Available online at http://www.nwas.org/ej/pdf/2011-EJ4.pdf.]

——, 2011b: The central European and Russian heat event of July–August 2010. *Bull. Amer. Meteor. Soc.*, **92**, 1285–1296, doi:10.1175/2011BAMS3174.1.

——, and R. Hart, 2001: Standardized anomalies applied to significant cold season weather events: Preliminary findings. *Wea. Forecasting*, **16**, 736–754, doi:10.1175/1520-0434(2001)016<0736:SAATSC>2.0.CO;2.

Hart, R. E., and R. H. Grumm, 2001: Using normalized climatological anomalies to rank synoptic-scale events objectively. *Mon. Wea. Rev.*, **129**, 2426–2442, doi:10.1175/1520-0493(2001)129<2426:UNCATR>2.0.CO;2.

Huang, J., J. Du, and W. H. Qian, 2015: A comparison between a generalized beta–advection model and a classical beta–advection model in predicting and understanding unusual typhoon tracks in eastern China seas. *Wea. Forecasting*, **30**, 771–792, doi:10.1175/WAF-D-14-00073.1.

Junker, N. W., R. H. Grumm, R. Hart, L. F. Bosart, K. M. Bell, and F. J. Pereira, 2008: Use of standardized anomaly fields to anticipate extreme rainfall in the mountains of northern California. *Wea. Forecasting*, **23**, 336–356, doi:10.1175/2007WAF2007013.1.

——, M. J. Brennan, F. Pereira, M. J. Bodner, and R. H. Grumm, 2009: Assessing the potential for rare precipitation events with standardized anomalies and ensemble guidance at the Hydrometeorological Prediction Center. *Bull. Amer. Meteor. Soc.*, **90**, 445–453, doi:10.1175/2008BAMS2636.1.

Lalaurette, F., 2003: Early detection of abnormal weather conditions using a probabilistic extreme forecast index. *Quart. J. Roy. Meteor. Soc.*, **129**, 3037–3057, doi:10.1256/qj.02.152.

Palmer, W. C., and R. A. Allen, 1949: Note on the accuracy of forecasts concerning the rain problem. U.S. Weather Bureau, 4 pp.

Qian, W. H., and Z. J. Zhang, 2012: Precursors to predict low-temperature freezing-rain events in southern China. *Chin. J. Geophys.*, **55**, 1501–1512.

——, and M. Jiang, 2014: Early signals of synoptic-scale atmospheric anomalies associated with the summer low temperature events in northeast China. *Meteor. Atmos. Phys.*, **124**, 33–46, doi:10.1007/s00703-013-0306-0.

——, J. Li, and X. L. Shan, 2013: Application of synoptic-scale anomalous winds predicted by medium-range weather forecast models on the regional heavy rainfall in China in 2010. *Sci. China Earth Sci.*, **56**, 1059–1070, doi:10.1007/s11430-013-4586-5.

——, X. L. Shan, H. Y. Liang, J. Huang, and C. H. Leung, 2014: A generalized beta-advection model to improve unusual typhoon track prediction by decomposing total flow into climatic and anomalous flows. *J. Geophys. Res. Atmos.*, **119**, 1097–1117, doi:10.1002/2013JD020902.

——, J. Du, X. L. Shan, and N. Jiang, 2015: Incorporating the effects of moisture into a dynamical parameter: Moist vorticity and moist divergence. *Wea. Forecasting*, **30**, 1411–1428, doi:10.1175/WAF-D-14-00154.1.

——, T. Yu, and J. Du, 2016: A unified approach to trace surface heat and cold events by using height anomaly. *Climate Dyn.*, doi:10.1007/s00382-015-2666-2, in press.

Schubert, H. W., S. A. Hausman, M. Garcia, K. V. Ooyama, and H. Kuo, 2001: Potential vorticity in a moist atmosphere. *J. Atmos. Sci.*, **58**, 3148–3157, doi:10.1175/1520-0469(2001)058<3148:PVIAMA>2.0.CO;2.

Smith, B. T., R. L. Thompson, J. S. Grams, C. Broyles, and H. E. Brooks, 2012: Convective modes for significant severe thunderstorms in the contiguous United States. Part I: Storm classification and climatology. *Wea. Forecasting*, **27**, 1114–1135, doi:10.1175/WAF-D-11-00115.1.

Van den Dool, H., 2007: *Empirical Methods in Short-Term Climate Prediction*. Oxford University Press, 215 pp.

Zhou, B., and J. Du, 2010: Fog prediction from a multimodel mesoscale ensemble prediction system. *Wea. Forecasting*, **25**, 303–322, doi:10.1175/2009WAF2222289.1.

Zsoter, E., 2006: Recent developments in extreme weather forecasting. *ECMWF Newsletter*, No. 107, Reading, United Kingdom, 8–17. [Available online at http://www.ecmwf.int/sites/default/files/elibrary/2006/14618-newsletter-no107-spring-2006.pdf.]